

SPECIAL

Community Climate System Model CCSM4

COLLECTION

## The Madden–Julian Oscillation in CCSM4

ANEESH C. SUBRAMANIAN,\* MARKUS JOCHUM,<sup>+</sup> ARTHUR J. MILLER,\* RAGHU MURTUGUDDE,<sup>#</sup>  
RICHARD B. NEALE,<sup>+</sup> AND DUANE E. WALISER<sup>@</sup>

\* Scripps Institution of Oceanography, University of California, San Diego, La Jolla, California

<sup>+</sup> National Center for Atmospheric Research, Boulder, Colorado

<sup>#</sup> University of Maryland, College Park, College Park, Maryland

<sup>@</sup> Jet Propulsion Laboratory, California Institute of Technology, Pasadena, California

(Manuscript received 14 January 2011, in final form 22 May 2011)

### ABSTRACT

This study assesses the ability of the Community Climate System Model, version 4 (CCSM4) to represent the Madden–Julian oscillation (MJO), the dominant mode of intraseasonal variability in the tropical atmosphere. The U.S. Climate Variability and Predictability (CLIVAR) MJO Working Group's prescribed diagnostic tests are used to evaluate the model's mean state, variance, and wavenumber–frequency characteristics in a 20-yr simulation of the intraseasonal variability in zonal winds at 850 hPa (U850) and 200 hPa (U200), and outgoing longwave radiation (OLR). Unlike its predecessor, CCSM4 reproduces a number of aspects of MJO behavior more realistically.

The CCSM4 produces coherent, broadband, and energetic patterns in eastward-propagating intraseasonal zonal winds and OLR in the tropical Indian and Pacific Oceans that are generally consistent with MJO characteristics. Strong peaks occur in power spectra and coherence spectra with periods between 20 and 100 days and zonal wavenumbers between 1 and 3. Model MJOs, however, tend to be more broadband in frequency than in observations. Broad-scale patterns, as revealed in combined EOFs of U850, U200, and OLR, are remarkably consistent with observations and indicate that large-scale convergence–convection coupling occurs in the simulated MJO.

Relations between MJO in the model and its concurrence with other climate states are also explored. MJO activity (defined as the percentage of time the MJO index exceeds 1.5) is enhanced during El Niño events compared to La Niña events, both in the model and observations. MJO activity is increased during periods of anomalously strong negative meridional wind shear in the Asian monsoon region and also during strong negative Indian Ocean zonal mode states, in both the model and observations.

### 1. Introduction

Four decades have passed since Madden and Julian made the pioneering discovery of a 40–50-day oscillation in the zonal winds in the tropics (Madden and Julian 1971, 1972). This discovery has led to numerous studies of a phenomenon now aptly called the Madden–Julian oscillation (MJO). Although MJO dynamics are still not fully understood (Madden and Julian 1994; Zhang 2005), MJO is known to interact with a panoply of climate phenomena across different spatial and temporal scales (Lau and Waliser 2005). Examples of MJO interactions

with some of these phenomena include its feedbacks with El Niño events (e.g., Marshall et al. 2009; Hendon et al. 2007; Zavala-Garay et al. 2005; Bergman et al. 2001; Kessler 2001; Takayabu et al. 1999), its feedbacks with the North Atlantic Oscillation (Cassou 2008), its impact on the onset and break of the Indian and Australian summer monsoons (e.g., Yasunari 1979; Wheeler and McBride 2005), its impact on the formation of tropical cyclones (e.g., Liebmann et al. 1994; Maloney and Hartmann 2000a,b), and its impact on the mean climate state (Sardeshmukh and Sura 2007). A better understanding and simulation of the MJO in models would help in studying these various climate phenomena, modeling them, and being able to predict these climate events better (Slingo and Inness 2005; Waliser 2006b).

To fully understand these important components of earth's climate, we need better knowledge of how the

Corresponding author address: Aneesh C. Subramanian, Scripps Institution of Oceanography, 9500 Gilman Dr., La Jolla, CA 92093-0224.  
E-mail: acsubram@ucsd.edu

MJO interacts with these components at various temporal and spatial scales (Lau and Waliser 2005). Yet, current climate models still have difficulty representing the MJO realistically. Numerous model intercomparison studies of their ability to capture the MJO have been published (Slingo et al. 1996; Waliser et al. 2003; Lin et al. 2006; Zhang et al. 2006; Sperber and Annamalai 2008; Kim et al. 2009), revealing how GCMs continue to struggle to represent MJO.

Slingo et al. (1996) showed in their study of the tropical intraseasonal variability using atmospheric GCM simulations forced by observed monthly-mean sea surface temperature (SST) that the Atmospheric Model Intercomparison Project (AMIP) models were unable to simulate the observed spectral peak in the 30–70-day-period band of the global (zonal wavenumber 1) equatorial 200-hPa velocity potential. Lin et al. (2006) analyzed MJO variability in 14 Coupled Model Intercomparison Project phase 3 (CMIP3) models, elucidating that only 2 models had MJO variance comparable to observations but that many other MJO features were lacking realism even in these models. Kim et al. (2009) studied a recent set of global models and noted that only two of them, the super-parameterized Community Atmosphere Model (SPCAM) and ECHAM4/Ocean Isopycnal Model (OPYC), yielded a respectable representation of MJO.

The aforementioned multimodel studies attempted to provide insight into what is important for MJO simulation by comparing the different physical parameterizations employed by models of differing MJO verisimilitude. A common theme throughout these studies is that a good MJO representation is influenced by the convection parameterization employed in the model, although many other factors come into play. As established global climate models continue to be improved with improved physics, they need to be validated for their performance in representing MJO variability because of its importance in influencing other climate phenomena.

Here we document how parameterizations in the National Center for Atmospheric Research (NCAR) Community Climate System Model (CCSM) affect the modeled MJO activity in long-term climate simulations. The latest version, CCSM4, has a novel deep convective momentum transport scheme, which profoundly alters the behavior of MJO events in the model. Our primary goal is to quantify the characteristics of MJO activity in CCSM4 according to the set of community diagnostics that has been developed to compare MJO simulations in climate models with observations [developed by the Climate Variability and Predictability (CLIVAR) Madden–Julian Oscillation Working Group 2008 (CL-MJOWG08); Waliser et al. 2009].

Recent work by Zhou et al. (2012) with a modified version of CCSM3 showed that MJOs were more realistic when including a convective momentum transport term

and a dilute plume approximation (DPA) in the convective parameterization scheme. Inclusion of the DPA improves the correlation between intraseasonal convective heating and intraseasonal temperature, which is critical for the buildup of the available potential energy. More realistic low-level background zonal winds over the Indo-Pacific warm pool improves the propagation speeds of intraseasonal variability in the convecting systems. We will show that the MJO is further improved in CCSM4 with 1° horizontal resolution compared to the previous versions of uncoupled CCSM studied by Zhang (2003) with the NCAR CCM3 using the modified convection parameterization scheme of Zhang and McFarlane (1995) at 3° resolution with prescribed SST; by Kim et al. (2009) with an uncoupled Community Atmosphere Model, version 3 (CAM3.5) at 2° resolution with prescribed SST; and by Zhou et al. (2012) with CCSM3.5 at 2° resolution.

Since the MJO is found here to be well represented in CCSM4, we also explore its interaction with other climate phenomena on interannual time scales. These include ENSO, the Indian monsoon, and the Indian Ocean zonal mode (IOZM) of SST. We demonstrate that the simulated MJO has key similarities with observed MJO for each of these climate modes. Since the record lengths are short, further analysis will be required to solidify this relationship in terms of causal linkages.

In section 2 we briefly describe the CCSM4 model used here, indicating the primary changes in the model setup from its previous version. The various observational datasets used in this study for the comparison of MJO in the model with those of nature are also presented. Section 3 contains the analysis of the model MJO, focusing on the structure and propagating features of the MJO in the model as compared to observations. In section 4 we identify relations between the model MJO and several climate indices from the model and observations. Section 5 summarizes the results.

## 2. Model simulations and validation data

### a. CCSM4

The CCSM is a general circulation climate model that couples the atmosphere, land, ocean, and sea ice components. Gent et al. (2011) gives an overview and a description of the CCSM version 4 climate simulation with 26 levels in the vertical,  $0.9^\circ \times 1.25^\circ$  horizontal atmosphere and land resolution, and nominally 1° ocean (with enhancement to 0.5° near the equator) and sea ice resolution. This version has numerous changes and improvements compared to version 3, as briefly documented here.

The core of the CAM version 4 has been changed from the spectral core used in CAM3 to the Lin-Rood finite

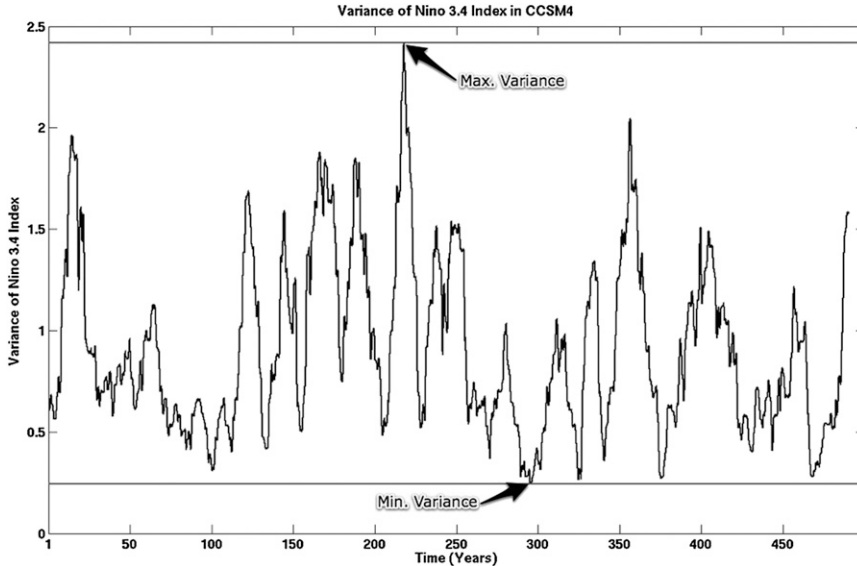


FIG. 1. A 10-yr sliding window variance of monthly-mean Niño-3.4 index for the 500-yr climate simulation of CCSM4.

volume core (Lin 2004). The CAM4 is the sixth generation of the NCAR atmospheric GCM and has again been developed through a collaborative process of users and developers in the Atmosphere Model Working Group (AMWG). In CAM4, changes to the moist physical representations center on enhancements to the existing Zhang and McFarlane (1995) deep convection parameterization.

The calculation of convective available potential energy (CAPE) assumes an entraining plume to provide the in-cloud temperature and humidity profiles used to determine buoyancy and related cloud closure properties. The modification is based on the conservation of moist entropy and mixing methods of Raymond and Blyth (1986, 1992). It replaces the standard nonentraining plume method used in CAM3 with a DPA to increase convection sensitivity to tropospheric moisture and to reduce the amplitude of the diurnal cycle of precipitation over land. Mixing occurs at all levels (not only at the cloud top) between the lowest model level and the neutral buoyancy level for a rising air parcel. According to DPA, air parcels seek the neutral buoyancy level and their specific entropy is conserved during the vertical motion. Mixing between the reference parcel and the free troposphere is dependent on an assumed entrainment rate. The representation of the MJO should benefit from increased sensitivity to tropospheric moisture because the observed occurrence of progressive premoistening is east of each MJO event's convecting maxima (Benedict and Randall 2007; Bechtold et al. 2008; Lin et al. 2008). This process may more readily occur in the model because DPA may inhibit some deep convection before the active phase of MJO and hence

cause the right conditions for large organization of deep convective systems into the MJO.

Subgrid-scale convective momentum transports (CMTs) have been added to the deep convection scheme following Gregory et al. (1997), which represents the compensation of CMTs by atmospheric subsidence. This was implemented in the model using the methodology of Richter and Rasch (2008). The CMT parameterization follows the mass flux approach and decomposes the product  $\overline{u'w'}$ , where  $u'$  and  $w'$  are unresolved perturbations to the zonal and vertical velocities, respectively, into three components: updraft, downdraft, and environment [see Eq. (3) in Gregory et al. 1997]. CMT affects tropospheric climate mainly through changes to the Coriolis torque. These changes result in improvement of the Hadley circulation during northern winter and it reduces many of the model biases (Neale et al. 2008). For example, the annual mean, the tropical easterly bias, subtropical westerly bias, and the excessive Southern Hemisphere mid-latitude jet, seen in CCSM3, are improved in CCSM3.5, as shown by Zhou et al. (2012). In combination, these modifications to the deep convection parameterization lead to significant improvements in the phase, amplitude, and spatial anomaly patterns of the modeled El Niño, also documented by Neale et al. (2008).

There also have been a number of changes to the ocean component of CCSM4, which are documented in Danabasoglu et al. (2012). For the tropical air-sea interface, the only change of relevance is the use of observed background diffusivities, which significantly reduces the tropical SST biases, which in turn reduce the tropical

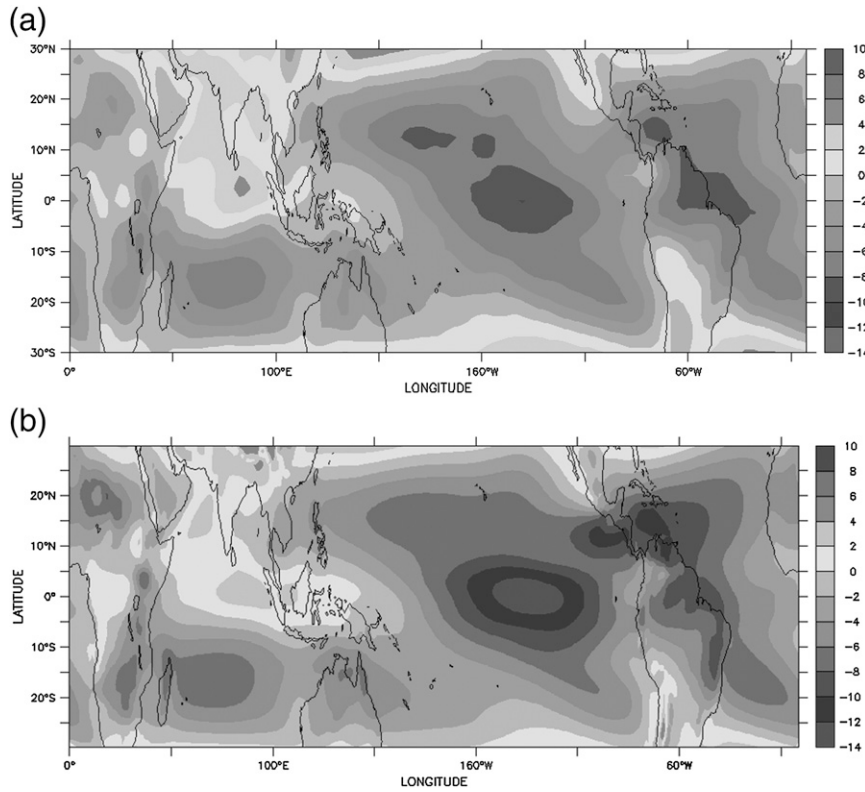


FIG. 2. (a) NCEP (20 yr) and (b) CCSM4 (20 yr) annual mean zonal 850-hPa winds in  $\text{m s}^{-1}$ . Period used in the calculations for NCEP is 1981–2000. A 20-yr period used in the model is a combination of the HENSO and LENSO 10-yr runs.

precipitation biases (Jochum 2009). Jochum (2009) and Richter and Rasch (2008) show that vertical diffusivity and CMT changes, respectively, tend to have opposite-signed but similar magnitude effects on annual mean tropical precipitation. The analysis to find which effect dominates the other in improving intraseasonal variability is beyond the scope of this study, yet it would be an important study to understand how the MJO is better represented and would help in improving the representation of the MJO further.

The NCAR CCSM4 group provided a 500-yr simulation as a control run under 1850 preindustrial conditions. Output from that run is saved as monthly means. Since the MJO has time scales comparable to that sampling, it was necessary to rerun CCSM4 and save the fields as daily means. Because of computational resource limitations, we were unable to rerun the model for the entire 500 yr. Since large ENSO events may influence the development and evolution of MJO, we decided to use two extreme 10-yr periods of ENSO behavior during the 500-yr run and then combine the analysis results for the two periods. One period has the maximum ENSO variance, and the other period has the minimum ENSO variance during the 500-yr base run. We treat the two 10-yr

runs as independent realizations of MJO behavior and compare them jointly (as a 20-yr model dataset) with National Centers for Environmental Prediction (NCEP) observations, thereby avoiding biasing the results toward the model's response in one state of ENSO variability. Additionally, we examine differences in MJO behavior in the two extreme ENSO regimes in section 4.

To establish two distinct ENSO regimes, we compute the ENSO Niño-3.4 index for the 500 yr from the CCSM base run monthly-mean model output. Then a sliding 10-yr window is employed to compute a time-varying variance for these 500 yr. The two 10-yr periods with the highest and lowest variability of ENSO are then identified, as shown in Fig. 1. Each case contains roughly 2.5 El Niño to La Niña transitions, with the amplitude of ENSO in the strong case being 2–3 times that of the weak variance case. The CCSM4 model was reinitialized from the base run CCSM4 for these periods (with perfect restarts) and the output was saved as 1-day averages to explore the high-frequency content of MJO in CCSM4. Saved fields included zonal and meridional winds, vertical velocity, specific humidity, relative humidity, temperature, geopotential, precipitation, and cloud fraction at all levels; plus net longwave, shortwave, latent and

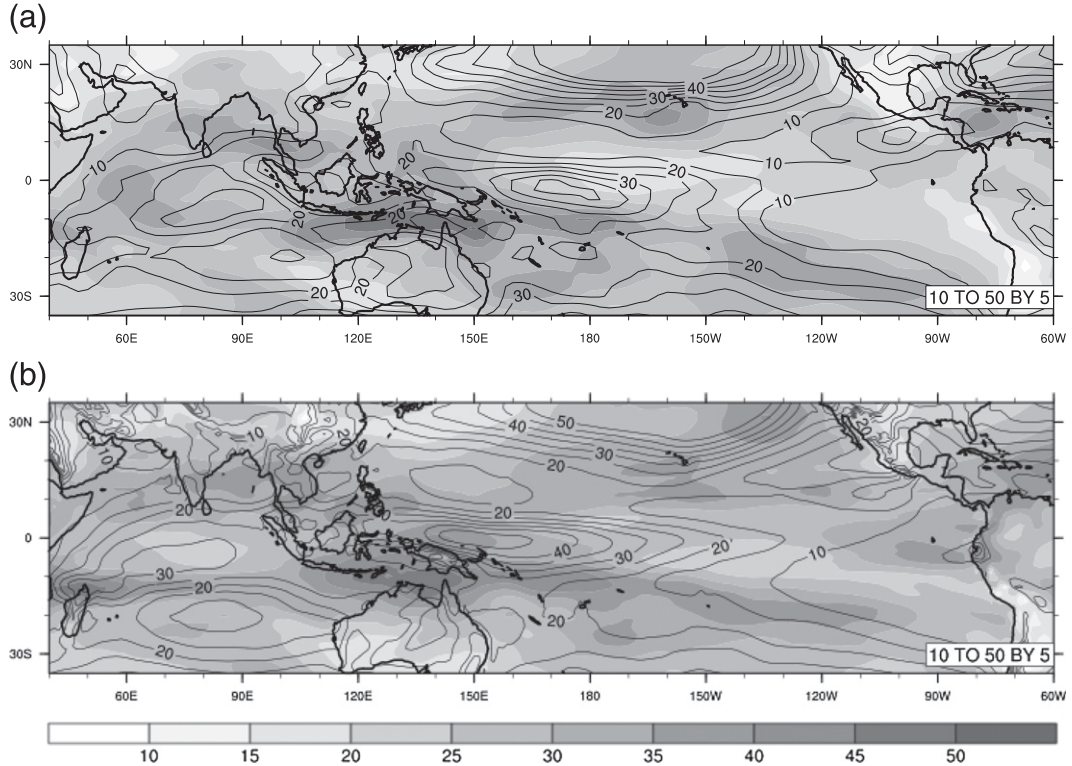


FIG. 3. (a) NCEP and (b) CCSM4 variance (line contours) in zonal 850-hPa winds in  $\text{m}^2 \text{s}^{-2}$  and the percentage ratio of the intraseasonal bandpassed (20–100 days) daily fields to the total variance (color contours). Period used in the calculations is 20 yr (1981–2000 for NCEP).

sensible heat fluxes at the surface and large-scale (liquid plus ice) precipitation rate. Hereafter, when necessary, the two 10-yr simulations of CCSM4 will be labeled HENSO for the high ENSO variability case and LENSO for the low ENSO variability case. The combined 20-yr run forms the basis for our MJO analysis.

#### b. Observational data

We validate the MJO characteristics in the 20-yr CCSM simulation against the Advanced Very High Resolution Radiometer (AVHRR) outgoing longwave radiation (OLR) (Liebmann and Smith 1996), which is a proxy for convective activity. We use rainfall from the Climate Prediction Center Merged Analysis of Precipitation (CMAP) (Xie and Arkin 1997) and the Global Precipitation Climatology Project (GPCP) (Huffman et al. 2001). The upper-tropospheric (200 hPa) and lower-tropospheric (850 hPa) zonal winds are from NCEP–NCAR reanalysis data (Kalnay et al. 1996).

### 3. MJO characteristics in CCSM4

#### MJO diagnostics

We adopt the CL-MJOWG08 strategy here and compute diagnostics for both boreal summer and winter

intraseasonal variability and mean state. The MJO band is isolated by running all fields through a 20–100-day Lanczos bandpass filter, following Waliser et al. (2009). The 20–100-day Lanczos bandpass-filtered data are dominated by the MJO signal, although it could have relatively small equatorial Rossby (ER) wave signals in addition to the MJO (Roundy et al. 2009). Although some previous works have demonstrated that some of these waves are systematically associated with the MJO, other equatorial Rossby waves are independent from the MJO and might influence some results (Kiladis et al. 2009).

As an important starting point, the mean state of the relevant variables is first validated. We did several comparisons of background state during the 20-yr model run versus observed climatology, and our results are largely consistent with those of Zhou et al. (2012) for CCSM3.5. For example, a comparison of the mean zonal 850-hPa winds in NCEP (observations) with the mean zonal 850-hPa winds for the CCSM runs reveals that the model simulations have structures that are comparable to the observed winds from NCEP. While the magnitude of the mean easterlies in the Pacific is 50% greater than observed, the westerlies over the Maritime Continent are nearly as strong as observed (Fig. 2). This extension of the zonal westerlies across the Maritime Continent can

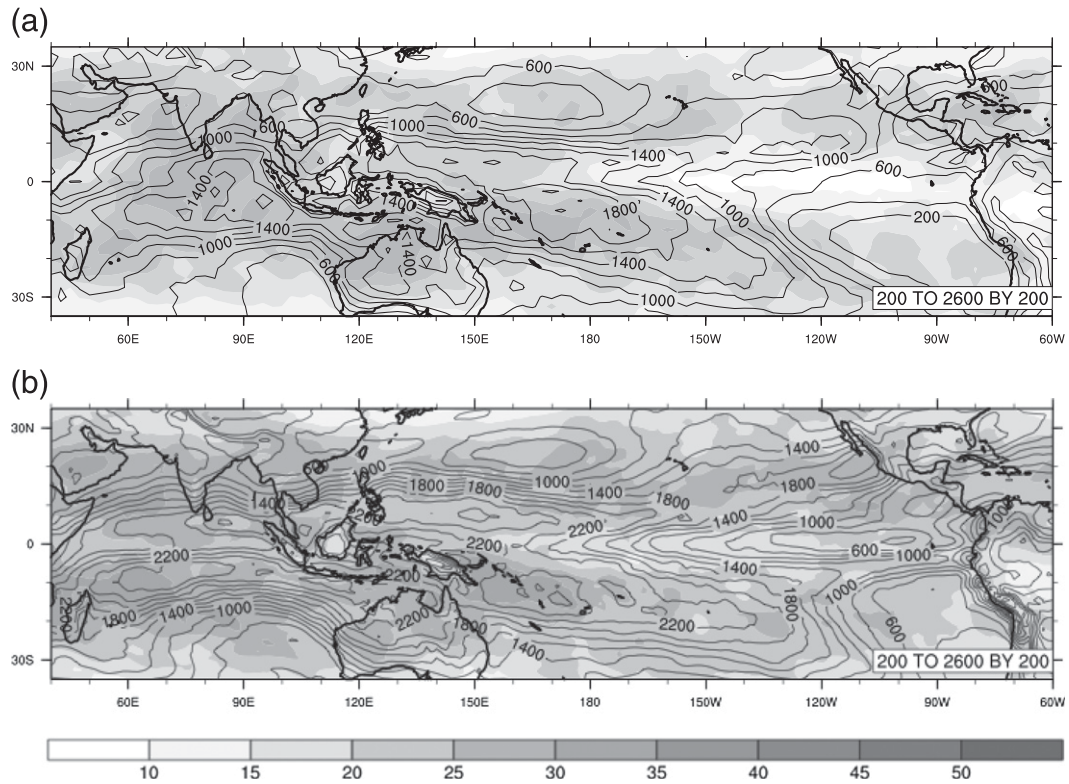


FIG. 4. (a) National Oceanic and Atmospheric Administration (NOAA) AVHRR satellite OLR and (b) CCSM4 variance (line contours) OLR in  $\text{W}^2 \text{m}^{-4}$  and the percentage ratio of the variance in the intraseasonal bandpassed (20–100 days) daily OLR fields to the total variance (color contours). Period used in the calculations is 20 yr (1981–2000 for NCEP).

favorably influence the propagation of the MJO into the western Pacific, as explained by Inness et al. (2003) for the third climate configuration of the Met Office Unified Model (HadCM3) and Zhou et al. (2012) for CCSM3.5.

### 1) LEVEL 1 DIAGNOSTICS

Level 1 diagnostics assess the dominant spatial and temporal scales as well as propagation direction of convection and 850-hPa zonal wind. These diagnostics provide a general evaluation of the broadband intraseasonal variability associated with MJO.

We first consider the winter 20–100-day variance of the zonal 850-hPa winds. The percentage of intraseasonal variance of zonal 850-hPa winds (color contours of Fig. 3) in NCEP is comparable to that of the model simulation. The structure of the intraseasonal variance pattern in the model is consistent with MJO characteristics, bearing minima in zonal wind variance along the equator in both the Indian and Pacific Oceans and a maximum variance over the Maritime Continent. The total variance of these winds in CCSM4 (line contours in Fig. 3) is also reasonably consistent with observations. Note, however, that at least at the air-sea interface, the Quick Scatterometer

(QuikSCAT) wind observations suggest that in the equatorial east Pacific, NCEP winds are approximately 30% too weak (Large and Yeager 2009).

Total OLR variance in CCSM4, shown by the line contours in Fig. 4, tends to be higher than in observations of AVHRR satellite OLR, especially over the Maritime Continent. The percentage of winter 20–100-day variance in model OLR has comparable values to observations over the Maritime Continent and in the western equatorial Pacific. However, in the MJO initiation region in the central Indian Ocean, the model has a smaller fraction of MJO OLR variance. Taken together with the zonal wind results, this may be indicative of a weaker coupling between the dynamic fields and convection in the MJO initiation regions of the Indian Ocean.

Hovmöller diagrams for zonal winds (averaged from 5°N to 5°S) are used to visually illustrate the eastward propagation of MJO signals. We chose one year from the model run with strong MJO activity and compared it to one observed year (1997) with a MJO to highlight the propagation characteristics (Fig. 5). These years both included La Niña events, when the western tropical Pacific SST was anomalously warm. In the model, eastward

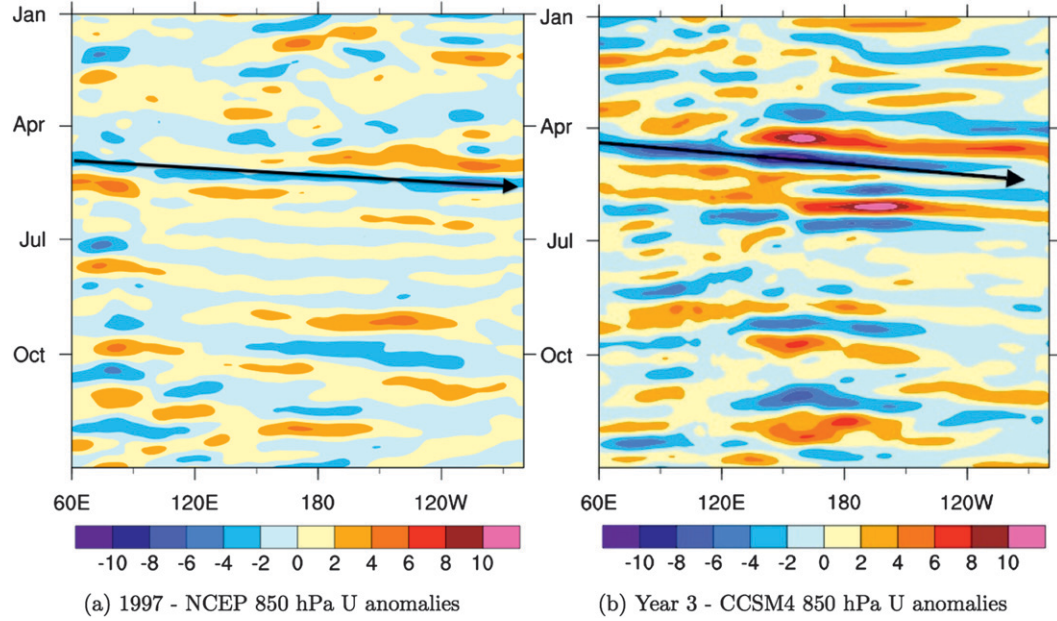


FIG. 5. Hovmöller plot of the intraseasonal (20–100 days) zonal 850-hPa winds of (a) NCEP in 1997 compared to that of intraseasonal zonal 850-hPa winds of year 3 of the (b) CCSM4 run. The arrow, which represents  $8 \text{ m s}^{-1}$ , is meant to guide the eye and shows eastward propagation.

propagation is evident during winter at speeds of about  $5\text{--}7 \text{ m s}^{-1}$ , which is comparable to the observed phase speeds. Events in both the model and observations originate in the Indian Ocean region and propagate around the globe. As also seen in observations, these events tend to weaken over the Maritime Continent and strengthen again in the western Pacific Ocean. Similar to observations, albeit more pronounced, the model MJO eastward-propagating activity in summer months is much weaker than in winter.

Power spectra of the wavenumber–frequency characteristics of observed winter MJO reveal a dominant peak for zonal wavenumber 1 and for a period of 60 days, with a broadband structure that extends to zonal wavenumbers 2 and 3 over periods of 30–80 days (Fig. 6). The model contains peaks in this band; however, the dominant peak at 60 days is somewhat stronger and more broadband than observations, and additional peaks occur at higher frequencies, suggesting that the model MJO is not as coherent as observations. Overall, CCSM4 contains significant eastward-propagating energy in the same frequency range for wavenumbers in the MJO band during the winter season, but the signals have more energy than observations. Also, the CCSM4 OLR does not have as strong of a peak in spectral power compared to observations (Fig. 6). The peak in the spectral power of the CCSM4 OLR is at higher frequencies than the intraseasonal band. This is consistent with the findings discussed in later sections that the dynamical

convective coupling in CCSM4 is weaker than that in nature. These spectra for CCSM4 show enhanced and more realistic energy at longer periods in the MJO band compared to frequency–wavenumber spectra computed by Zhang (2003) for CCM3, which exhibit dominant peaks at approximately 40 days and zonal wavenumber 1.

## 2) LEVEL 2 DIAGNOSTICS

Level 2 diagnostics assess the coupling between the dynamic and thermodynamic variables. In addition to single-variable spectral calculations, cross-spectral calculations are computed to quantify the coherence and phase relationships between different variables. The cross-spectral plots demonstrate that the thermodynamic and dynamic effects are coupled.

Figure 7 shows the coherence squared and the phase between equatorial OLR and 850-hPa zonal winds for the symmetric components of the two fields (Hendon and Wheeler 2008). The symmetric component physically represents the symmetric dynamics about the equator, which is a first-order characteristic of the observed MJO. The left panels show the spectrum across a broad range of scales, while the right panels show a more detailed view of the scales of the MJO.

Observations exhibit a high degree of coherence and an approximately  $90^\circ$  phase lag between convection and 850-hPa winds for zonal wavenumbers 1–3 in the 30–80-day band (Figs. 7a,b). Although climate models are well known to have difficulty simulating this feature

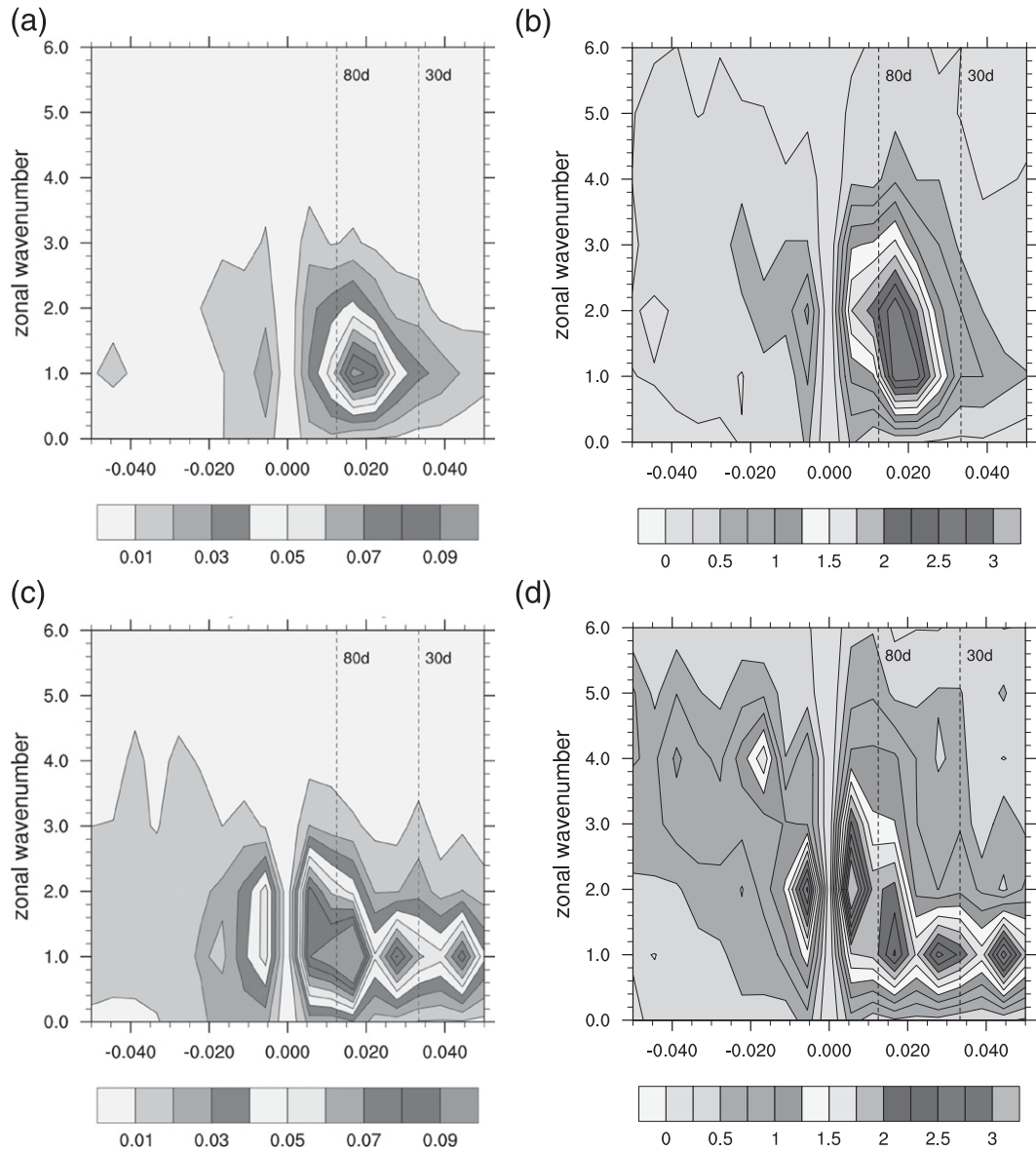


FIG. 6. November–April wavenumber–frequency spectra of  $10^{\circ}\text{N}$ – $10^{\circ}\text{S}$  averaged daily zonal 850-hPa winds of (a) NCEP (1981–2000) and (b) CCSM4 (20 yr of HENSO and LENSO runs), and daily OLR fields of (c) NOAA satellite OLR (1981–2000) and (d) CCSM4. Individual spectra were calculated for each year and then averaged over 20 yr of data. Only the climatological seasonal cycle and time mean for each November–April segment were removed before calculation of the spectra. Units for the zonal wind spectrum are  $\text{m}^2 \text{s}^{-2}$  per frequency interval per wavenumber interval. The bandwidth is  $(180 \text{ day})^{-1}$ .

(e.g., Zhang et al. 2006; Zhou et al. 2012), CCSM4 exhibits strong coherence in this low-wavenumber band, with lags similar to observations. However, for wavenumber 1, model coherency peaks at higher frequencies near 30-day periods compared to the 40-day peak for observations (Figs. 7c,d). This modeled coherency relation suggests that convectively coupled MJOs occur in the model for wavenumber 1. The model's spread of coherency into higher frequencies at wavenumber 1,

however, suggests that more linear Kelvin wave activity, with a convective signature, is present in CCSM4 than in observations (Roundy 2008). To distinguish whether the coherency peak at wavenumber 1 is due to a simple Kelvin wave, Fig. 8 shows the antisymmetric part of the coherency relationship for the MJO band, which should have no imprint of a linear Kelvin wave. Observations reveal significant coherency (0.15–0.35) for wavenumber 1. The model also has significant coherency (0.05–0.15)

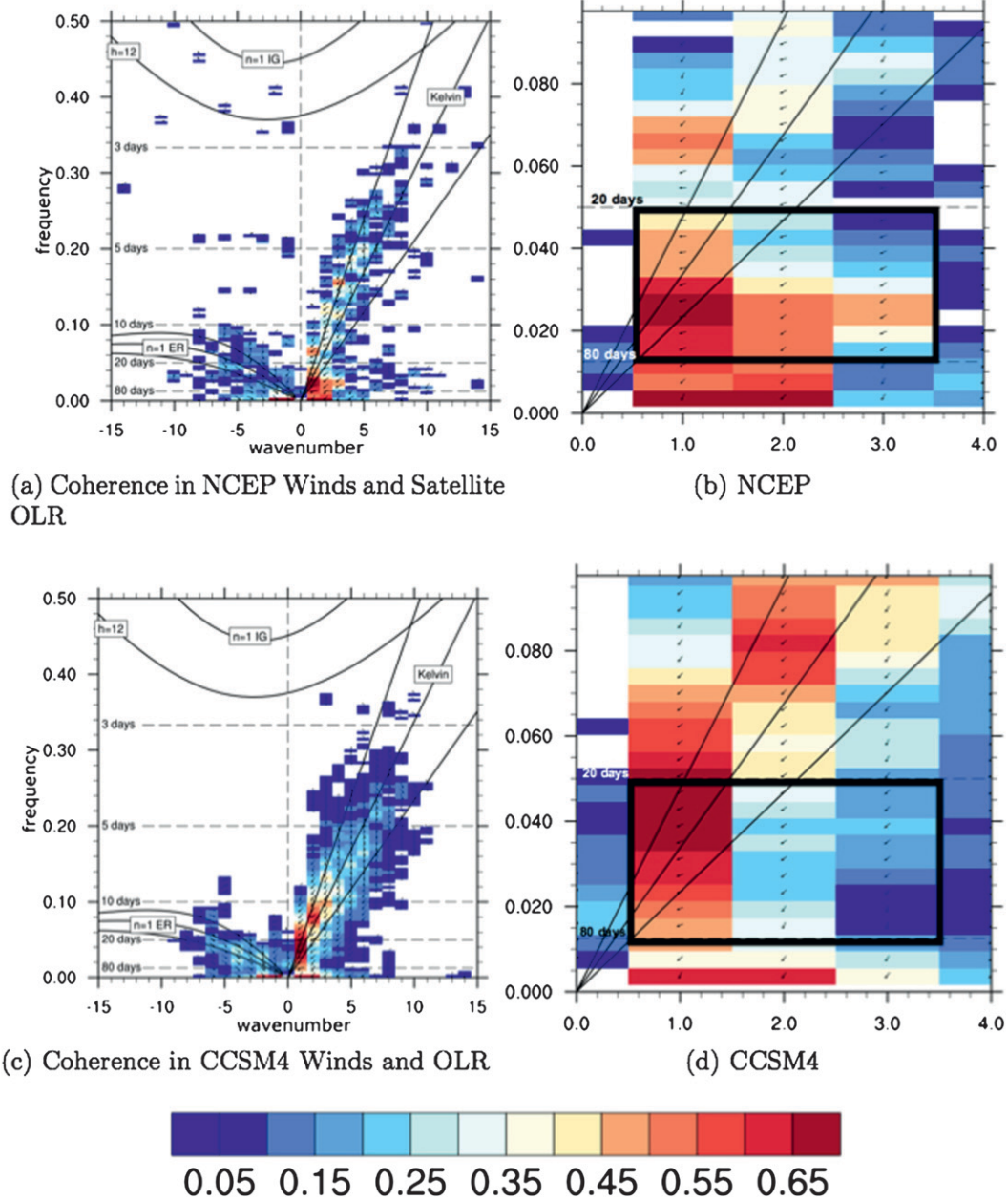


FIG. 7. Coherence squared (colors) and phase lag (vectors) between zonal winds at 850-hPa winds and OLR are shown for (a) NCEP winds and satellite OLR and (c) CCSM4 winds and OLR; (b) and (d) are expanded views of the MJO-relevant parts of the spectra. Only the symmetric spectra are shown here. Cross spectra are calculated using daily data during all seasons on 256-day-long segments, with consecutive segments overlapping by 206 days. Colors represent coherence squared between OLR and U850, and vectors represent the phase by which wind anomalies lag OLR anomalies, increasing in the clockwise direction. A phase of  $0^\circ$  is represented by a vector directed upward. Dispersion curves for the ( $n = -1$ ) Kelvin,  $n = 1$  ER, and ( $n = 1$ ) inertia-gravity waves corresponding to three equivalent depths ( $h = 12, 25$ , and  $50$  m) in the shallow-water equations are overlaid (black contours). MJO is defined as the spectral components within zonal wavenumbers 1–3 and having periods of 20–80 days, as marked by the black box in the right panels.

in this band, although somewhat weaker than observations. This antisymmetric structure is clearly indicative of convectively coupled MJO behavior at wavenumber 1.

At wavenumbers 2 and 3 in Figs. 7c,d, CCSM4 has much lower convergence-convection coherency in the MJO 40–80-day-period band than observations. Instead, CCSM4 exhibits high convergence-convection coherency

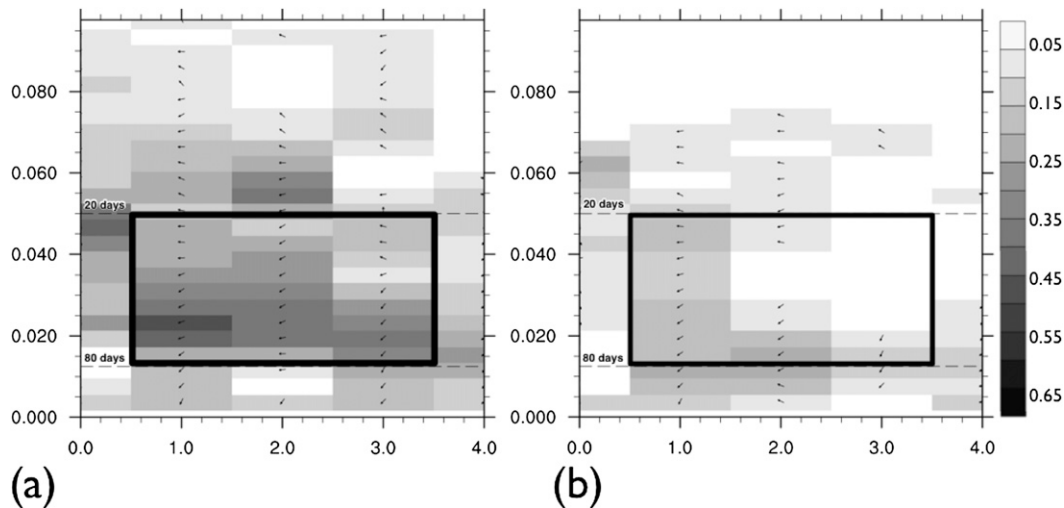


FIG. 8. Antisymmetric spectrum of coherence squared (colors) and phase lag (vectors) between zonal winds at 850-hPa winds and OLR are shown for (a) NCEP winds and satellite OLR and (b) CCSM4 winds and OLR as expanded views of the MJO-relevant parts of the spectra. Cross spectra are calculated using daily data during all seasons on 256-day-long segments, with consecutive segments overlapping by 206 days. Colors represent coherence squared between OLR and U850, and vectors represent the phase by which wind anomalies lag OLR anomalies, increasing in the clockwise direction. A phase of  $0^\circ$  is represented by a vector directed upward. MJO is defined as the spectral components within zonal wavenumbers 1–3 and having periods of 20–80 days as marked by the black box in the right panels.

for these two wavenumbers at 10–15-day periods, which is indicative of Kelvin waves bearing a convective signature, since the coherence falls along the linear dispersion curves. The antisymmetric part of the model spectrum (Fig. 8) has no significant coherence at these periods and wavenumbers, supporting this interpretation. This part of the response is associated with intraseasonal oscillations that travel at speeds of  $10\text{--}22 \text{ m s}^{-1}$ , which are faster than the typical observed MJO phase speed of  $5 \text{ m s}^{-1}$ . This weakly energetic and fast propagation at wavenumbers 2 and 3 in CCSM4 may be associated with a lack of coupling between MJO and oceanic Kelvin waves in the central equatorial Pacific, which Roundy and Kravitz (2009) identified as an important mechanism for slowing and amplifying higher-wavenumber-observed MJO in this region.

The faster phase speed of MJO in CCSM is also evident in Fig. 9b, which shows the lag correlation between the convection and the dynamic winds for observations and the model. Model MJO activity tends to propagate to the Maritime Continent, where it breaks up and then reorganizes over the western Pacific and continues propagating across the Pacific slightly faster and even further than observations suggest.

We next use the Wheeler and Hendon (2004, hereafter WH04) technique to extract the dominant MJO spatial and temporal modes. Combined EOFs (CEOFs), using OLR, U850, and U200, each bandpassed to the

20–100-day-period band, are computed. This multivariate approach isolates the convective and baroclinic zonal wind signature of the MJO. We specifically focus on the evaluation of 1) the vertical baroclinic structure in the winds and the lag in OLR and convection, with the winds depicting a moving convection and convergence system; 2) the evolution of the MJO life cycle in the model simulations; and 3) the MJO life cycle composite depicting the various phases in the MJO evolution with respect to convection and the convergence zone.

The two leading modes in both the model and observations correspond to MJO patterns and time scales. Figure 10 shows the  $15^\circ\text{N}\text{--}15^\circ\text{S}$  average of the CCSM4 MJO CEOFs 1 and 2 for all three variables. Compared to the observed modes shown in Fig. 11, mode 2 from observations corresponds to mode 1 of the CCSM4. The longitudinal location of the maxima, minima, and zero crossings of all three variables correspond well between the model and observations. Likewise, observational mode 1 corresponds well to the structures seen in mode 2 of the CCSM. The magnitudes of the CEOFs in the model are about 40% smaller than the same in the observed fields. We conclude that in this period band, MJO phasing between physical variables in CCSM4 is remarkably consistent with observations but are weaker in magnitude. The partitioning of variance in the combined EOF analysis is as follows: OLR (18%), U200 (37%), and U850 (50%) for the first two combined EOFs. The

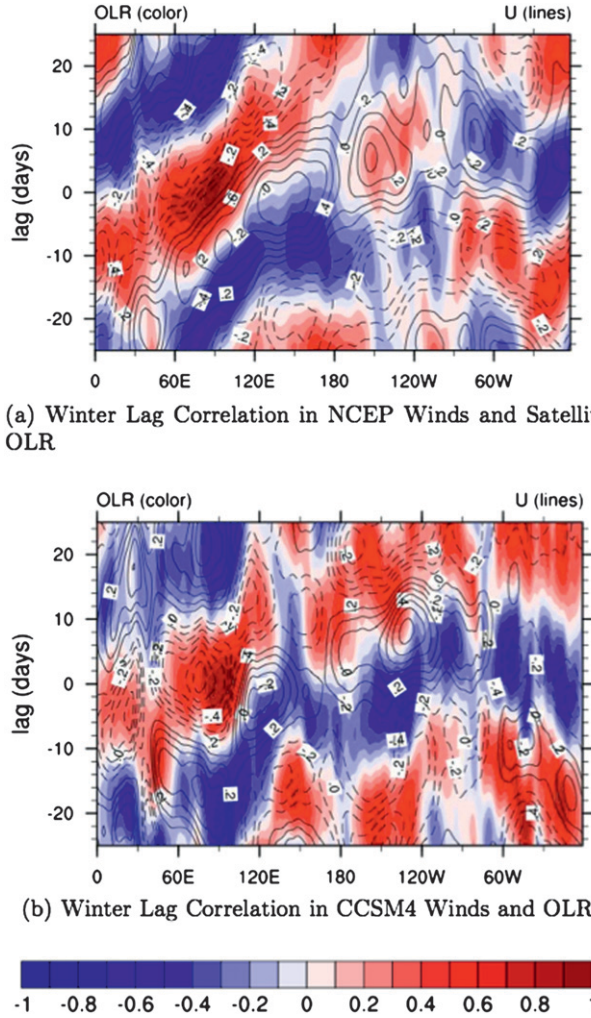


FIG. 9. November–April lag-longitude diagram of 10°N–10°S averaged intraseasonal OLR anomalies (colors) and intraseasonal 850-hPa zonal wind anomalies (contours) correlated against intraseasonal OLR at the Indian Ocean reference box (10°S–5°N, 75°–100°E) for (a) observations and (b) CCSM4.

variance explained by the principal components (PCs) individually is as follows: PC1—OLR (10%), U200 (21%), and U850 (26%); and PC2—OLR (8%), U200 (16%), and U850 (24%). This too is remarkably consistent with the observed values of Waliser et al. (2009), namely, PC1<sub>obs</sub>—OLR (13%), U200 (22%), and U850 (32%); and PC2<sub>obs</sub>—OLR (16%), U200 (24%), and U850 (23%).

The lag correlation between PC1 and PC2 provides a measure of temporal coherency for the eastward-propagating MJO. These are calculated for year-round fields for CCSM4 and shown in Fig. 12a. The familiar S shape found in observations occurs (Waliser et al. 2009), with peak correlations of roughly 0.6 occurring at  $\pm 8$ -day lags in CCSM4 compared to a peak of 0.7 at

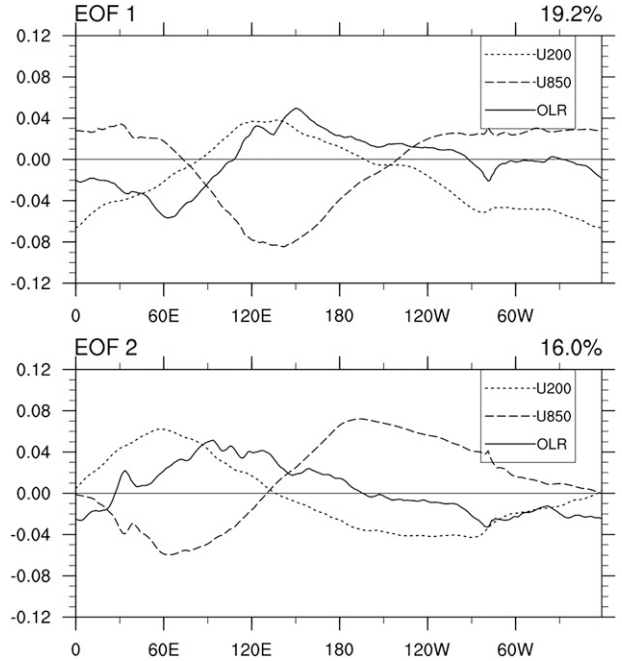


FIG. 10. All-season multivariate (a) first and (b) second CEOF modes of 20–100-day 15°S–15°N averaged zonal wind at 850 and 200 hPa, and OLR from the 20-yr CCSM4 run. Total variance accounted for by each mode is shown in parenthesis at the top of each panel.

$\pm 10$ -day lags in observations. This indicates the dominant period is roughly 32 days in the model but roughly 40 days in observations, consistent with the higher power seen at high frequencies in CCSM4 in the power spectra of Fig. 6. The phase relationship indicates that the multivariate EOF1 and EOF2 are a quadrature pair. This pair of leading EOFs represents coherent eastward propagation of MJO. It is a well-known challenge for GCMs to properly represent this coherent quadrature pair. Further, to verify whether the extracted MJO modes are a physically meaningful mode of variability and are distinct from noise, we project the leading EOFs derived from filtered data onto unfiltered data (after only removing the seasonal cycle). The power spectrum of the unfiltered PCs, shown in Fig. 12b, yields a prominent peak at MJO time scales, very similar to Waliser et al. (2009) except for the higher energy in the model spectral “shoulder” at 20–30-day periods. This increases our confidence in the diagnostics that the modes of variability obtained are indeed meaningful.

The two leading multivariate EOFs can also be used to derive a composite MJO life cycle for boreal summer or winter, following WH04. The composite is constructed by selecting full fields of U850, U200, and OLR during the time intervals when MJO is strongly excited. The amplitude of the MJO is defined by  $PC1^2 + PC2^2$  after

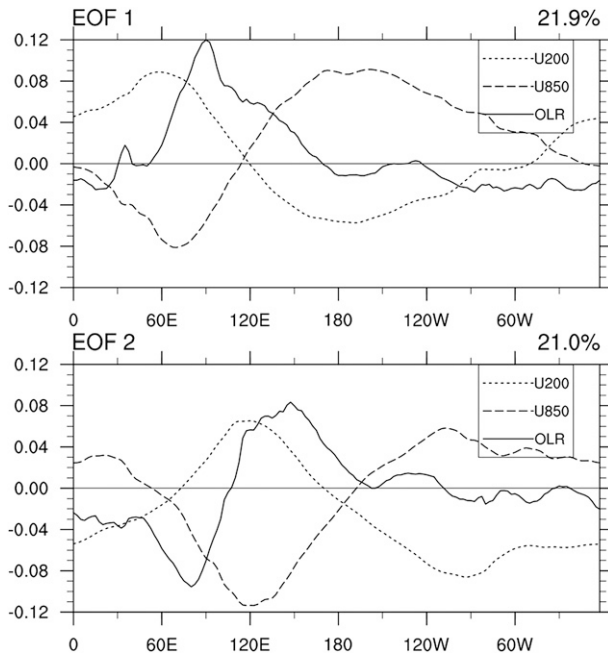


FIG. 11. All-season multivariate (a) first and (b) second CEOF modes of 20–100-day 15°S–15°N averaged zonal wind at 850 and 200 hPa from NCEP, and OLR from the NOAA satellite for 1980–99. Total variance accounted for by each mode is shown in parentheses at top of each panel.

PC1 and PC2 are normalized to unit standard deviation. The time intervals for the composite fields are defined as times when the MJO index exceeds 1.5 (Fig. 18). The amplitudes for the MJO index during the two model time periods HENSO and LENSO are shown (Fig. 18). The phase of the MJO is defined as  $\text{atan}(\text{PC2}/\text{PC1})$ . For each of the eight phases, composites are generated by averaging across all days that exceed the specified amplitude threshold. The composite life cycle for the boreal winter MJO in the CCSM4 simulation is shown in Fig. 13. The same for observations is shown in Fig. 14.

In general, CCSM4 generates a realistic succession of phases associated with MJO (Fig. 13), very similar to those from observations (Fig. 14) in many respects. The model phases differ from those in observations in a few details. The convection in phase 3 in the model composite occurs off the equator rather than over it as in observations (consistent with the variance plots of OLR in Fig. 4). From phase 3 to phase 5, westerlies increase in the eastern Indian Ocean and intensify convection over the Maritime Continent, but not as strongly as observations. The intensity of the OLR in the model is also lower and more widespread in model phases 3–6 compared to those in observations. Compared to a similar composite shown by Zhou et al. (2012) for CCSM3.5, CCSM4 exhibits a more realistic OLR pattern over the

Indian Ocean region during the initiation phase and more coherent propagating components across the Maritime Continent. Likewise, the phase composites for CCSM4 exhibit much more organized patterns of MJO propagation than found by Zhang (2003) for CCM3.

We next consider the nature of the precipitation in the intraseasonal band. Figure 15 shows the variance in the intraseasonal precipitation from the model and GPCP observations. The model precipitation variance is about 50% greater than that in observations, suggesting that the convectively coupled intraseasonal bands of MJO generate excessive precipitation in the model. The intraseasonal variance of the diabatic heating caused by convection parameterized in the model has a spatial pattern that is similar to the variance of the precipitation (Fig. 16). This supports the idea that the excessive precipitation in the model is due to large-scale convective systems (such as the MJO) in the intraseasonal band. In the Indian Ocean initiation region of MJO, during phases 2 and 3 of the composite MJO, the ratio of large-scale precipitation resolved by the model to the Zhang–McFarlane parameterized precipitation is shown in Fig. 17. Roughly 30%–35% of the precipitation during MJO initiation in the Indian Ocean is resolved by the model and hence is consistent with a large-scale intraseasonal convective system propagating rather than the small-scale convection dominating the precipitation.

In summary, CCSM4 exhibits an energetic eastward-propagating signal with MJO-like properties in the 20–100-day-period band and the 1–3 zonal wavenumber band. The model MJO has somewhat stronger amplitudes and faster propagation speeds than observations. For wavenumber 1, cross-spectral measures of convergence–convection relationships in the MJO period band are similar in strength to observations and indicate convectively coupled MJO is occurring. The more broad-banded coherency in frequency suggests that additional activity associated with Kelvin waves with a convective signature also occurs in the model. This interpretation is even more evident for wavenumbers 2 and 3, which exhibit convergence–convection coherency for high frequencies that are outside the MJO band.

Compared to other global coupled models, CCSM4 exhibits relatively high skill in simulating these intra-seasonal oscillations. As compared to the models analyzed in Kim et al. (2009), CCSM4 has pronounced energy in the MJO band and is comparable to the best models listed, namely, ECHAM4 and SPCAM. Also, the period and energy of the simulated ENSOs in CCSM4 are much improved compared to its previous CCSM versions. As shown in Kim et al. (2009), the period with maximum energy has shifted from 200 days for CCSM3.5 to the intraseasonal period of 70 days for CCSM4.

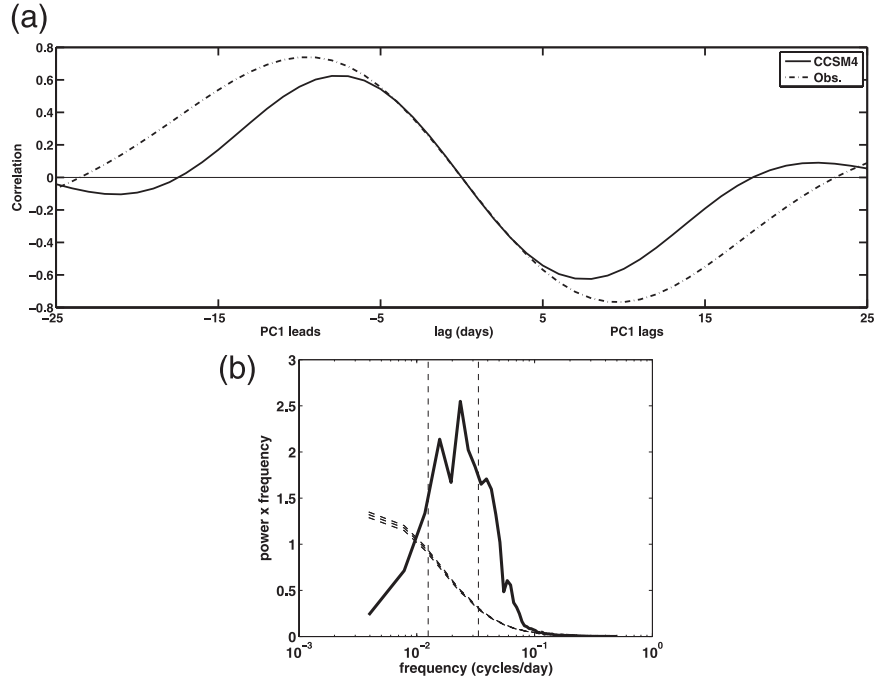


FIG. 12. (a) Lag correlation between PC1 and PC2 of multivariate EOF analysis of the intraseasonal zonal winds at 850 and 200 hPa, and intraseasonal OLR anomalies from the CCSM4 run and observations. (b) Power spectral density of the CCSM4 PC projected onto the unfiltered data. Dashed lines show the red noise spectrum and upper 90% and 95% confidence limits on this red noise spectrum.

Additionally, the intraseasonal wavenumber peak has broadened to include wavenumbers 1–3 from mainly being at wavenumber 1, with intraseasonal spectral power levels having increased by about 50% in CCSM4 compared to CCSM3.5. Besides improved parameterizations, some of the improvement over the results of Kim et al. (2009) is likely due to the higher resolution used here ( $1^\circ$  vs  $2^\circ$ ) and the inclusion of full ocean coupling (rather than prescribed SST).

Since the phase of the OLR and winds in CCSM correspond well with the structure of MJO, the simulations of MJO can therefore be analyzed for relations with other climate phenomena, such as ENSO and the monsoons, to attempt to understand their dynamical interactions. We next execute some preliminary attempts at addressing these issues.

#### 4. Relations of MJO to other climate phenomena

##### a. MJO–ENSO relations

El Niño–Southern Oscillation is the strongest inter-annually varying phenomenon in the tropical coupled ocean–atmosphere system. The MJO is the strongest intraseasonal-varying phenomenon in the tropical coupled

ocean–atmosphere system. Although both of these phenomena have most of their energy in widely separated time scales, they have been shown to interact and modulate each other since both of them involve large-scale tropical convection, large-scale atmospheric circulation changes, and teleconnections to other global weather phenomena (Kessler and Kleeman 2000; Hendon et al. 2007; Neale et al. 2008; Marshall et al. 2009; Pohl et al. 2010).

The strength of the MJO varies year to year, and some of this variability in the west Pacific has been linked to ENSO. For example, equatorial zonal wind variability on MJO time scales has been noted to affect the subsequent development of ENSO events (Bergman et al. 2001; Kessler 2001; Hendon et al. 2007; Tang and Yu 2008). The impact of ENSO on MJO variability, however, is less clear. Lin and Li (2008) suggested that MJO activity is sensitive to whether ENSO is in a developing or decaying state during summer. Roundy and Kravitz (2009) also showed a sensitivity of MJO behavior to oceanic state because MJO interactions with oceanic Kelvin waves associated with ENSO in the western equatorial Pacific.

The possible relationships between MJO and ENSO states are explored here by relating the periods when MJO is “active” (MJO index exceeds 1.5) to three states of ENSO, defined by the Niño-3.4 index exceeding a

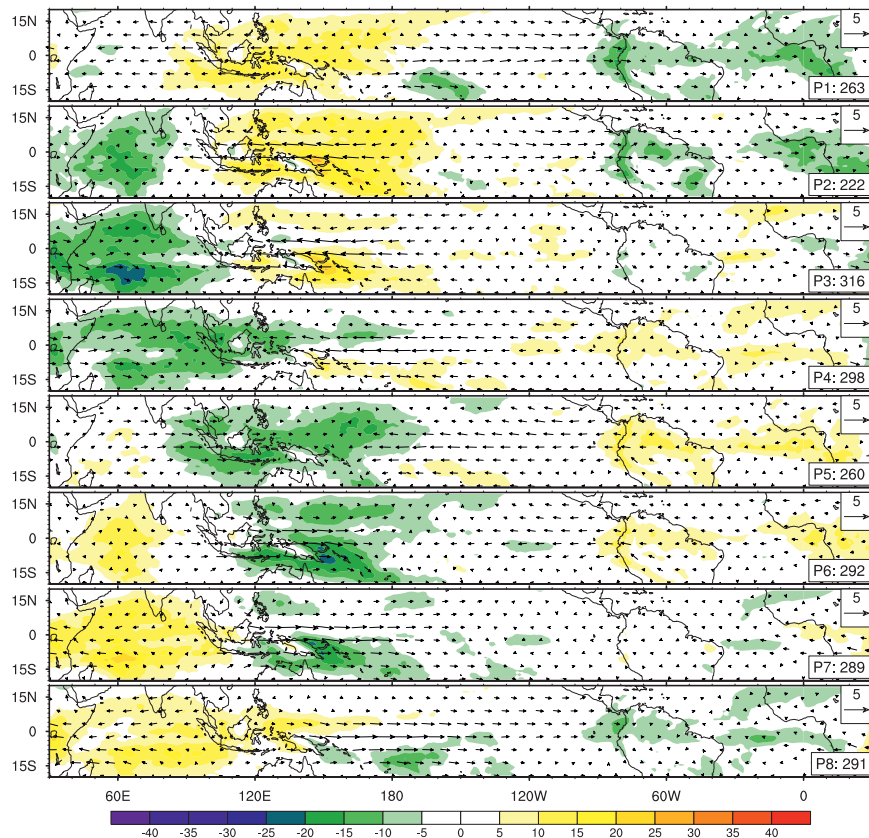


FIG. 13. Composite November–April 20–100-day OLR (color, in  $\text{W m}^{-2}$ ) and 850-hPa wind anomalies (vectors) as a function of MJO phase for the 20-yr CCSM run. Reference vector in units of  $\text{m s}^{-1}$  is shown at the top right. Number of days used to generate the composite for each phase is shown at the bottom right of each panel.

threshold for at least 3 months (El Niño when the index exceeds 0.5 and La Niña when the index is less than  $-0.5$  and neutral otherwise). Figure 18 shows the results for both the model run and observations, along with 1) the percentage of time MJO is *active* during the ENSO states and 2) the average *strength* of MJO during the ENSO states when MJO is active. Considering the El Niño and the La Niña states, both the model and observations have a tendency to produce enhanced MJO activity during the warm events compared to cold ENSO events. The model MJO also tends to produce lower-amplitude activity during cold events but this relation does not occur in observations, where MJO amplitude is fairly uniform across ENSO states. Since there are very few of these ENSO events in the model and observations during this 20-yr period, these results are only suggestive. Further work needs to be done to address these MJO–ENSO issues more deeply.

Reasons for the higher activity of MJO during warm events may involve the background zonal wind field and the SST in the tropical Indian Ocean and western Pacific

Ocean. Stronger westerly winds, which are often associated with warm events in these regions, appear to support the development of MJO activity in CCSM3 by pacing the propagation speed of developing convective events, as suggested by Zhou et al. (2012). The expanded range of the warm pool region during warm events has also been shown by Hendon et al. (2007) to establish favorable conditions for MJO to propagate farther to the east in the western and central Pacific, thereby sustaining MJO. Both of these effects are consistent with the enhanced MJO activity and amplitude found in our analysis for both the model and observations during warm events. Taken together, these two effects are physically consistent with the idea that the warm SST in the central Pacific and the suppressed Walker cell associated with warm events can enhance MJO activity (Hendon et al. 2007), as suggested in our analysis.

There is also evidence from other studies that MJO influences the ENSO cycle (Kessler and Kleeman 2000; Newman et al. 2009; Marshall et al. 2009; Lau 2005). These studies have shown that the MJO does not cause

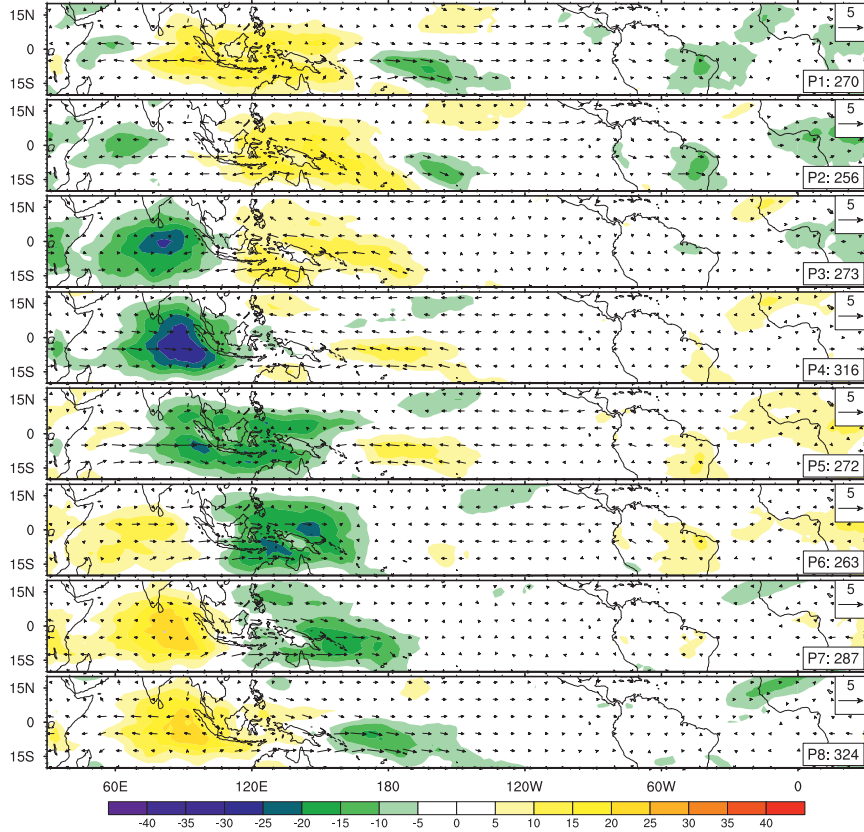


FIG. 14. Composite November–April 20–100-day OLR (color, in  $\text{W m}^{-2}$ ) and 850-hPa wind anomalies (vectors) as a function of MJO phase for observations from 1980 to 1999. Reference vector in units of  $\text{m s}^{-1}$  is shown at the top right. Number of days used to generate the composite for each phase is shown at the bottom right of each panel.

El Niño or La Niña, but they can change the development and intensity of the ENSO events. In particular, Roundy (2008) showed how MJO can enhance the development of El Niño episodes by significantly altering the low-level wind field that can, in turn, result in variations in the ocean subsurface conditions and later sea surface temperature. In our model runs, higher MJO activity was indeed associated with warm events, which supports that concept and possibly indicates that cool ENSO events are less affected by MJO. Additional model runs are needed to properly isolate these possible feedbacks.

We studied and compared the two 10-yr model cases with HENSO and LENSO, but the MJO variability in these two runs was not significantly different. The mean fields of the zonal winds, meridional winds, and OLR were nearly indistinguishable. Minor differences were found in the variance of 850-hPa zonal winds, which tended to peak in the Maritime Continent and the central Pacific region during the HENSO period, whereas during the LENSO episode the peak is constrained to the Maritime Continent. The Indian Ocean zonal winds

and OLR had somewhat weaker intraseasonal variance during LENSO as compared to the HENSO period. The power spectral density of the zonal 850-hPa winds in the Indian Ocean contained higher peaks in the 20–100-day band in the HENSO case. In the western Pacific region, the power spectral density of the zonal 850-hPa winds contained broader and higher peaks in the LENSO case. The wavenumber–frequency spectra revealed more power in the 30–40-day winds in the LENSO case and less power in the 60–100-day winds. The phase speed of propagation of the MJO along the equator, gauged by the lag correlation plots of OLR and U850 as in Fig. 9, was closer to the observed for HENSO. Our results for high and low ENSO variance cases did not appear to be statistically significant, given the short 10-yr record length and small number of ENSO events that occurred within them.

#### b. MJO–monsoon relations

MJO interacts considerably with the circulation and variability of Asian summer monsoon (Annamalai and Slingo 2001; Waliser et al. 2003; Waliser 2006a). In the

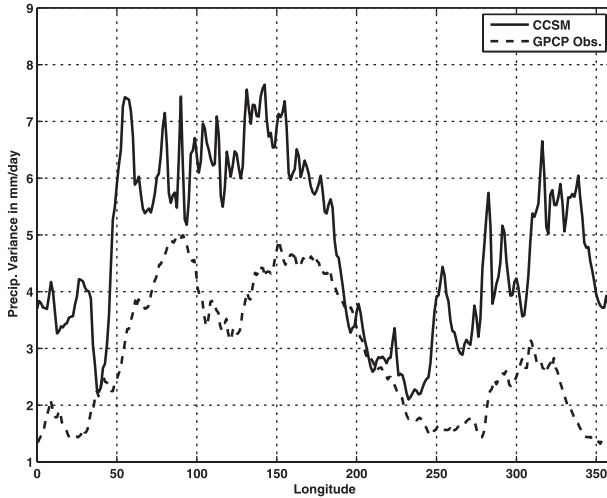


FIG. 15. Variance in (20–100 days) intraseasonal precipitation averaged over 5°N to 5°S for 20 yr of the CCSM4 run and GPCP observations (1996–2006).

monsoon season, intraseasonal disturbances associated with the MJO tend to propagate in a northeast direction and strongly influence the active and break monsoon rainfall cycles over the South and East Asian continent (Yasunari 1979; Annamalai and Slingo 2001; Waliser 2006b), including the genesis of synoptic systems (Goswami et al. 2003). Although it is still an area of research whether most of the intraseasonal variability associated with the northward-propagating intraseasonal oscillations are independent of the MJO or are generated by them, it is known that the MJO during boreal summer does influence other weather phenomena in the South Asian region such as hurricanes (Camargo et al. 2009; Bessafi and Wheeler 2006). Since the early work of Yasunari (1979), our knowledge about the MJO influence on the boreal summer monsoon has been enhanced many fold because of the availability of satellite data.

Indices have been defined to quantify monsoon variability, such as the precipitation indices averaged over the subcontinent and the dynamical monsoon indices designated as the Webster–Yang index [ $\mathbf{U}_{850}^* - \mathbf{V}_{200}^*$ , where  $\mathbf{U}^*$  is the zonal wind anomaly, averaged over the region from 40°E to 0°–20°N, 110°E (WYI; Webster and Yang 1992)] and the monsoon Hadley index [ $\mathbf{U}_{850}^* - \mathbf{V}_{200}^*$ , where  $\mathbf{V}^*$  is the meridional wind anomaly, averaged over the region from 70°E to 10°–30°N, 110°E (MHI; Goswami et al. 1999)]. These two indices measure the variability in the dynamical zonal shear and meridional shear over the north Indian Ocean, respectively.

The possible relationships between the MJO index and the strength of the meridional shear are explored by relating the periods when the MJO index exceeds 1.5 to three states of the MHI, depending on whether the MHI

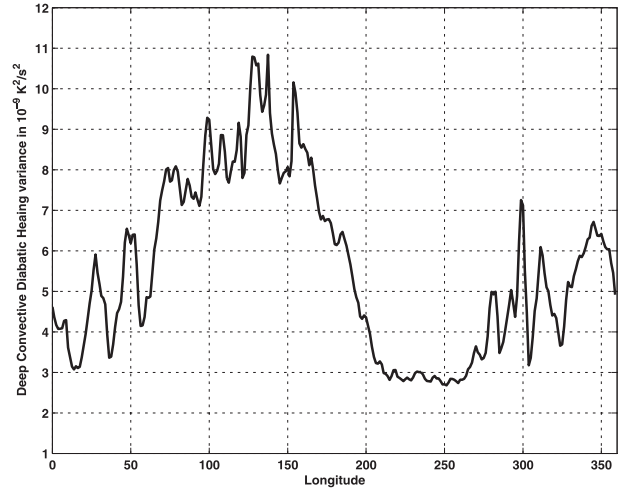


FIG. 16. Variance in (20–100 days) intraseasonal diabatic heating due to deep convection parameterized by the Zhang–McFarlane scheme in the CCSM4 averaged over 5°N–5°S.

is greater than 1, between 1 and –1, or less than –1 for the positive, neutral, and negative states, respectively. Figure 19 shows these results for both the model and observations, along with 1) the percentage of time when MJO is active during the MHI states and 2) the average strength of MJO during the MHI states when MJO is active. The results, for both the model and observations, show that MJO preferentially occurs during negative MHI conditions. MJO amplitudes do not show any consistent relationship with the MHI state in either the model or observations. We also explored the relation between the MJO index and the strength of the zonal

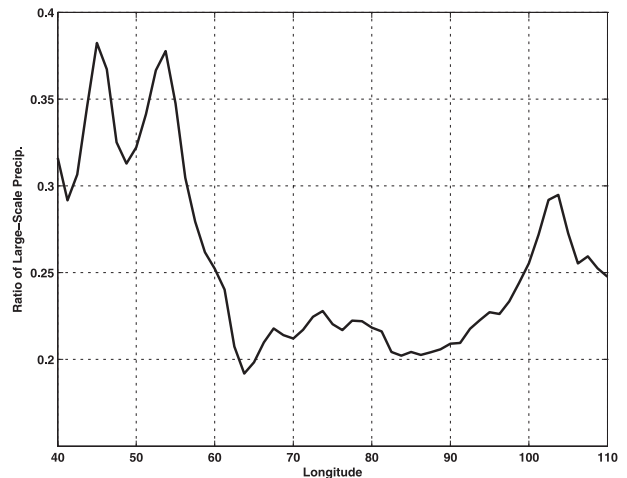


FIG. 17. Percentage ratio of large-scale (nonparameterized) precipitation to total precipitation in the CCSM4 averaged over 5°N–5°S during phases 2 and 3 of MJO when (20–100 days) intraseasonal convection is predominantly in the Indian Ocean.

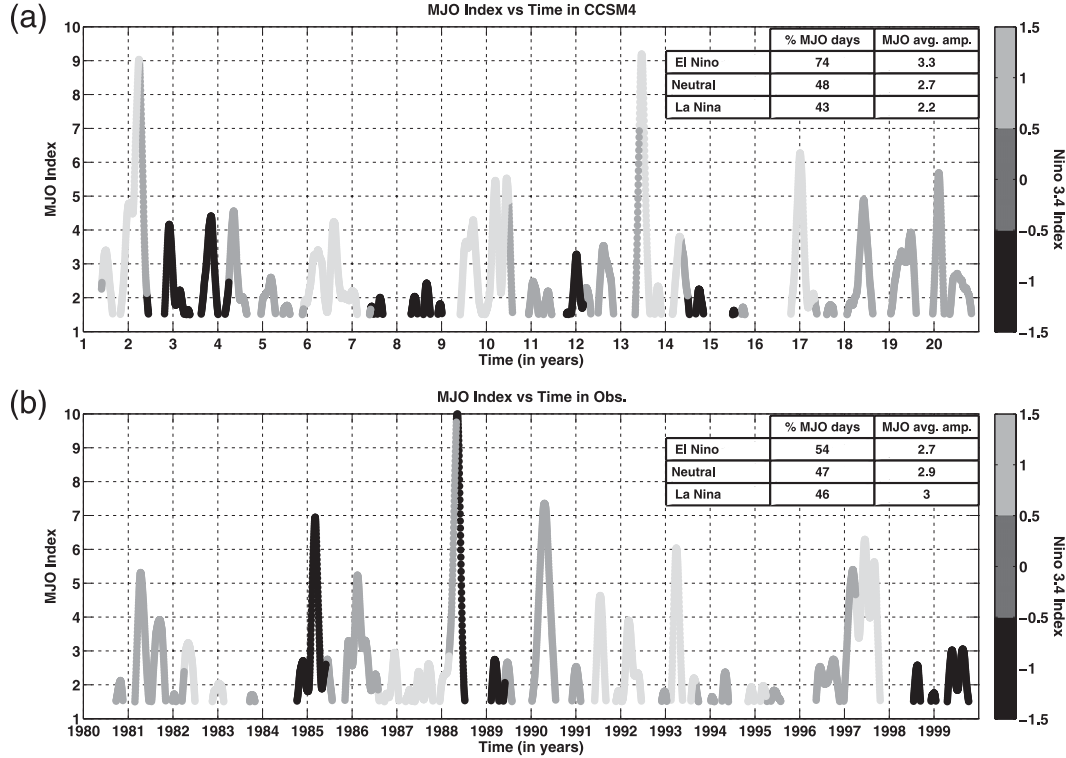


FIG. 18. Daily MJO index and ENSO Niño-3.4 index in the (a) 20-yr simulations compared to (b) observed MJO index and ENSO Niño-3.4 index (from NOAA). Warm (cold) events are defined as being persistently above (below) 0.5 ( $-0.5$ ) for at least 3 months. During the observation period, there were a total of 2400 El Niño days (1299 MJO active days), 3390 neutral days (1593 MJO days), and 1410 La Niña days (646 MJO days). During the 20 yr of the CCSM4 simulations, there were a total of 1950 El Niño days (1437 MJO days), 3420 neutral days (1646 MJO days), and 1830 La Niña days (784 MJO days).

shear, based on the WYI, but no consistent relation occurred between the model and observations in the results (Table 1).

The reason for the stronger activity of MJO during periods of negative meridional shear (northerly winds aloft and southerly winds below) is likely because of the enhanced vertical motion in the Hadley circulation over the Indian Ocean (Annamalai et al. 2003). In this situation, MJO is sustained and energized by the anomalous updrafts and convection over the warm equatorial Indian Ocean waters. Positive meridional shear, in contrast, implies increased subsidence and reduced convective activity, which suppresses MJO generation.

The role of Indian Ocean SST anomalies on the South Asian monsoons has been a topic of several studies (e.g., Yuan et al. 2008; Krishnamurthy and Kirtman 2003; Goswami and Mohan 2001). Indian Ocean variability is known to be strongly seasonal and is related to ENSO variability. Many studies have focused on the role of the IOZM and its potential effect on the Asian monsoon (Saji et al. 1999; Webster et al. 1999; Annamalai et al. 2003). The IOZM defined in Annamalai et al. (2003) is

shown to correlate significantly with the Asian summer monsoon in a few studies (Behera et al. 1999; Yuan et al. 2008). Yet, it is still an area of intense debate. Studies show that the IOZM is most significantly correlated with the local Hadley cell, which influences the Asian monsoons (Slingo and Annamalai 2000). The IOZM has been noted to influence MJO activity as well (Rao et al. 2007; Ajayamohan et al. 2008). Kug et al. (2009) showed that the high-frequency atmospheric variability in the Indian Ocean is modulated by IOZM events and that MJO and synoptic eddies become significantly energetic during negative IOZM events.

The possible relationships between the MJO and IOZM states are explored here by relating the periods when the MJO index exceeds 1.5 to three states of the IOZM index (positive, neutral, and negative phases, when the IOZM index is greater than 1, between 1 and  $-1$ , and less than  $-1$ , respectively), defined by Annamalai et al. (2003), as shown in Fig. 20. Both the model and observations reveal a tendency for higher MJO activity during negative IOZM states. The model also has higher-amplitude MJO during these times, but this aspect of the relationship is not

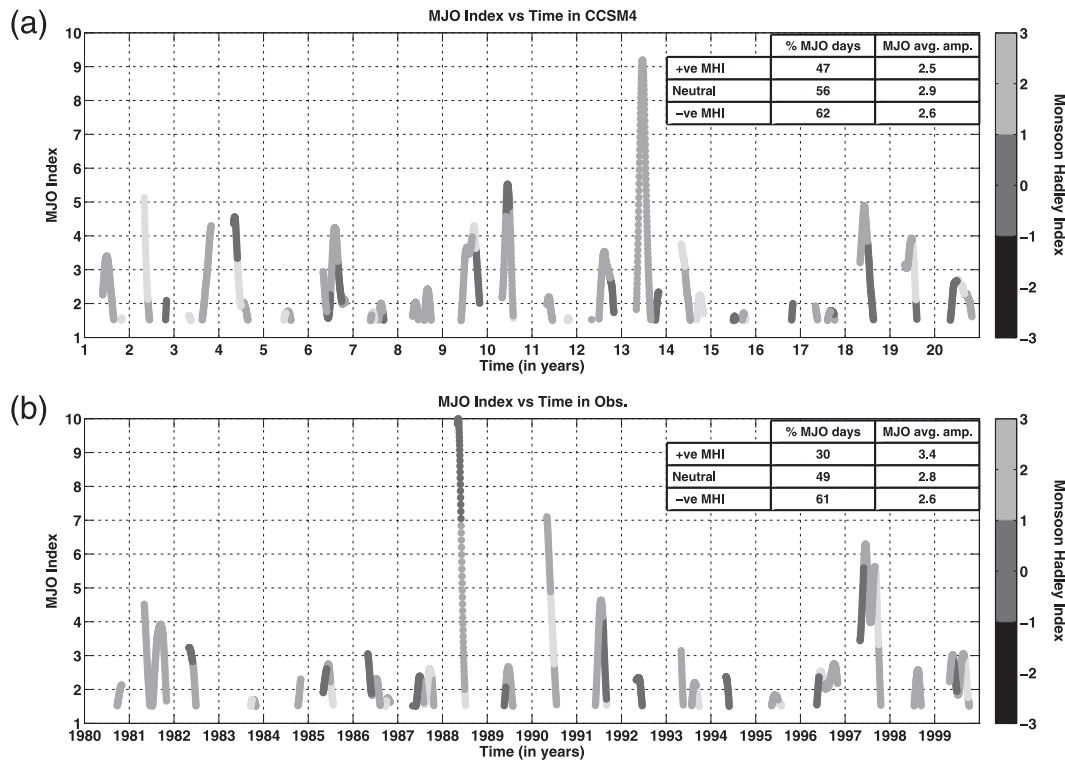


FIG. 19. MJO index shaded by the intensity of the monsoon Hadley index in (a) the CCSM4 in the 20-yr simulations and in (b) observations from 1980 to 2000. Shading indicates periods corresponding to different MHI states, as indicated by the color bar. Neutral periods are when the absolute value of the MHI index is less than 1.

found in observations. These results are consistent with the idea that a negative IOZM event, which has anomalously warm ocean surface in the eastern and central Indian Ocean, would set up anomalous westerlies in the equatorial Indian Ocean and enhanced convection in the eastern Indian Ocean. Both of these processes sustain and support strong MJO activity (Inness et al. 2003; Zhou et al. 2012; Waliser et al. 2009). However, since the run is of limited duration, this result is only suggestive of the dynamic interplay between MJO and IOZM, and it motivates further research on the issue.

## 5. Summary and discussion

Simulating and forecasting the MJO is of central importance to the global climate and weather community, especially as models continue to increase resolution

and resolve the various processes that contribute to intraseasonal variability. Yet, most climate models today fail to simulate even the large-scale features of the MJO. In this study, we evaluate the performance of a 20-yr run of CCSM4 in reproducing the primary characteristics of MJO, based on diagnostics established by the CL-MJOWG08.

The CCSM4 model produces coherent, broadband, and energetic patterns in eastward-propagating intra-seasonal zonal winds and OLR in the tropical Indian and Pacific Oceans that are generally consistent with MJO characteristics. Strong peaks occur in power spectra and coherence spectra with periods between 20–100 days and zonal wavenumbers between 1 and 3. Model MJOs, however, tend to be more broadband in frequency than observation, with higher frequencies being associated with zonal wavenumbers in the MJO band. For wavenumber

TABLE 1. Percentage of days of active MJO during different phases of the zonal shear (quantified by WYI) in the northern Indian Ocean, and the average amplitude of the MJO is shown during these different phases.

	% MJO days (CCSM4)	(Observation)	MJO avg amplitude (CCSM4)	(Observation)
Positive WYI	48	58	2.9	3.0
Neutral	40	36	2.7	2.7
Negative WYI	65	51	2.7	2.8

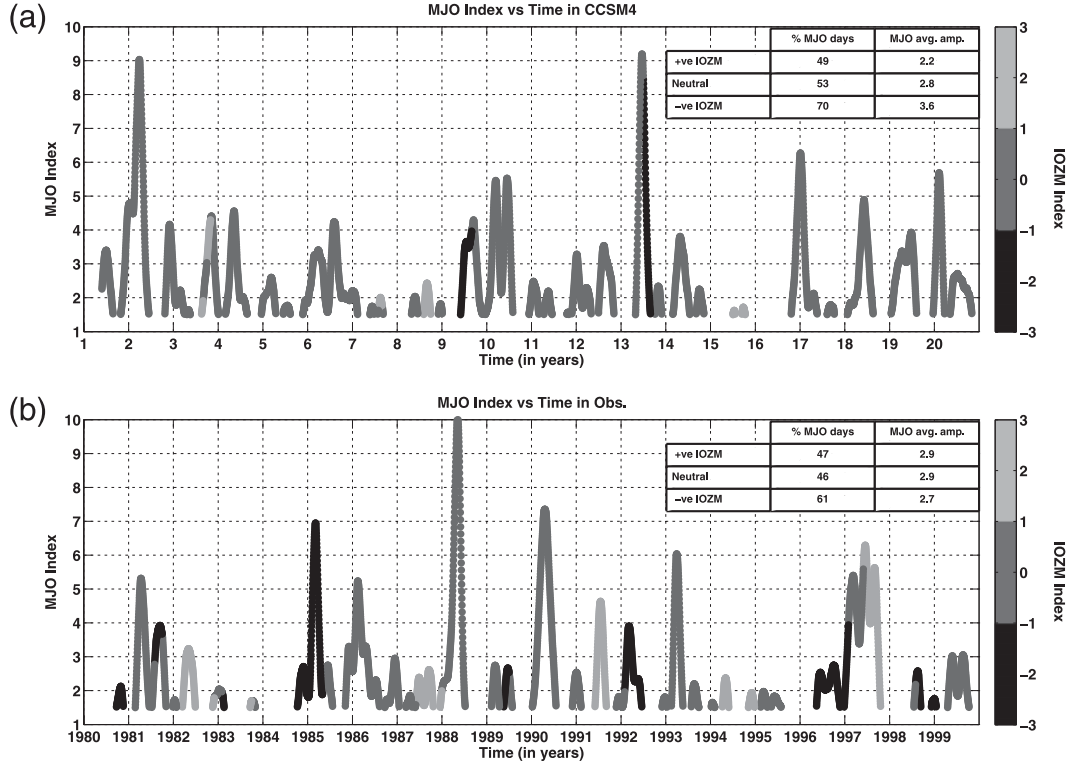


FIG. 20. As in Fig. 19, but shaded by the intensity of the IOZM index.

1, cross-spectral measures of convergence–convection relationships in the MJO band are similar in strength to observations and indicate convectively coupled MJOs are occurring. The more broadband coherency in frequency suggests that additional activity associated with Kelvin waves with a convective signature also occur in the model. This interpretation is even more evident for wavenumbers 2 and 3, which exhibit convergence–convection coherency for high frequencies that are outside the MJO band. Broadscale patterns, as revealed in combined EOFs of U850, U200, and OLR, however, are remarkably consistent with observations and indicate that convective coupling occurs in the simulated MJO.

Relations between MJO and other climate phenomena were explored as well. Possible links between MJO and ENSO state, monsoonal flow, and Indian Ocean zonal mode were identified. A tendency to produce enhanced MJO activity during warm ENSO events compared to cold ENSO events was noted in both the model and observations. The model MJO also tends to produce lower-amplitude activity during strong cold events but this relation does not occur in observations. MJO also preferentially occurs during negative meridional shear conditions in the northern Indian Ocean region, as defined by the monsoon Hadley index. There was no

obvious relation between MJO occurrence and the zonal shear over the northern Indian Ocean region, as defined by Webster–Yang index. A tendency for higher MJO activity during strongly negative IOZM states is also seen in the model and observations. The model also has higher-amplitude MJO during these times, but this relationship is not found in observations.

The interplay between climate modes of variability, such as ENSO, the Asian monsoon, the IOZM and MJO, can lead to complicated relationships among these modes (e.g., Ashok et al. 2001; Ihara et al. 2007; Cherchi et al. 2007). Although such multimode interactions were not extensively explored here, the results suggest that CCSM4 is suitable for these types of studies. Since Walker's (1923, 1924) original suggestion that ENSO modifies the Asian monsoon, many researchers have demonstrated an inverse relationship between the two modes (Webster and Yang 1992; Ju and Slingo 1995; Annamalai and Liu 2005; Bracco et al. 2006; Annamalai et al. 2007). The CCSM4 reproduces this observed relationship (Table 2), but further study is needed to link this behavior to MJO activity and identify potential feedbacks among these three climate modes (e.g., Chakraborty and Krishnamurti 2003; Pai et al. 2011). For example, Ashok et al. (2001) show that the frequent occurrence of IOZM events can weaken the inverse relationship between the ENSO and

TABLE 2. Regression coefficient (coeff) for MHI and Niño-3.4, and WYI and Niño-3.4.

Regression coef (CCSM4)	(Observation)	Intercept (CCSM4)	(Observation)	$R^2$ (CCSM4)	(Observation)
MHI	-0.4	-0.2	0	0	0.4

the monsoon. Also, Slingo and Annamalai (2000) suggest that very strong warm ENSO events (such as 1997/98) can alter the Walker cell over the Indian Ocean and shift the ITCZ northward, thereby increasing monsoon rainfall and destroying the inverse relationship between ENSO and the monsoon. MJO could thereby be simultaneously affected in multiple ways when these types of large-scale climate mode interactions occur and possibly feed back onto the entire coupled system. In CCSM4, the preference for enhanced MJO activity during the negative regimes of the monsoon Hadley circulation, warm ENSO events, and negative IOZM events substantiates previous research that the MJO convective phases in the Indian Ocean are associated with above-normal convection appearing throughout the equatorial Indian Ocean and corresponding to an anomalous increase in subsidence over the monsoon trough region (Pai et al. 2011).

These results illustrate how well CCSM4 simulates MJO behavior in a wide range of background climate states. Longer runs, targeted numerical experiments, and additional diagnostic calculations are needed to further clarify the detailed dynamical processes that control MJO variability, structure, and linkages to other climatic phenomena in this system.

**Acknowledgments.** This research forms a part of the Ph.D. dissertation of AS. We gratefully acknowledge funding from ONR (Grant N00014-10-1-0541), NOAA (Grant NA17RJ1231 through ECPC), DOE (Grant 25322A), and NSF (Grant OCE06-47815). The views expressed herein are those of the authors and do not necessarily reflect the views of these agencies. This research was initiated during a visit by AS to NCAR funded by the SUNNY (Scripps/UCSD/NCAR's New and Young) Program. AS acknowledges NCAR's computational support for simulations conducted for this study. We thank Paul Roundy and the other two referees for their careful reviews and important comments that significantly improved the manuscript. We also thank Mitch Moncrieff for his erudite comments and criticism of this work. AS extends heartfelt thanks to Dennis Shea for his help with NCL and for providing some of the observational data used in this analysis, and to Bruce Cornuelle for his many invaluable gems of wisdom on science and data analysis. Part of this research was carried out at the Jet Propulsion Laboratory, California Institute of Technology, under a contract with the National Aeronautics and Space Administration.

## REFERENCES

- Ajayamohan, R. S., S. A. Rao, and T. Yamagata, 2008: Influence of Indian Ocean dipole on poleward propagation of boreal summer intraseasonal oscillations. *J. Climate*, **21**, 5437–5454.
- Annamalai, H., and J. Slingo, 2001: Active/break cycles: Diagnosis of the intraseasonal variability of the Asian summer monsoon. *Climate Dyn.*, **18**, 85–102.
- , and P. Liu, 2005: Response of the Asian summer monsoon to changes in El Niño properties. *Quart. J. Roy. Meteor. Soc.*, **131**, 805–831.
- , R. Murtugudde, J. Potemra, S. Xie, P. Liu, and B. Wang, 2003: Coupled dynamics over the Indian Ocean: Spring initiation of the zonal mode. *Deep-Sea Res. II*, **50**, 2305–2330.
- , K. Hamilton, and K. R. Sperber, 2007: The South Asian summer monsoon and its relationship with ENSO in the IPCC AR4 simulations. *J. Climate*, **20**, 1071–1092.
- Ashok, K., Z. Guan, and T. Yamagata, 2001: Impact of the Indian Ocean dipole on the relationship between the Indian monsoon rainfall and ENSO. *Geophys. Res. Lett.*, **28**, 4499–4502.
- Bechtold, P., M. Köhler, T. Jung, F. Doblas-Reyes, M. Leutbecher, M. J. Rodwell, F. Vitart, and G. Balsamo, 2008: Advances in simulating atmospheric variability with the ECMWF model: From synoptic to decadal time-scales. *Quart. J. Roy. Meteor. Soc.*, **134**, 1337–1351.
- Behera, S., R. Krishnan, and T. Yamagata, 1999: Unusual ocean-atmosphere conditions in the tropical Indian Ocean during 1994. *Geophys. Res. Lett.*, **26**, 3001–3004.
- Benedict, J., and D. Randall, 2007: Observed characteristics of the MJO relative to maximum rainfall. *J. Atmos. Sci.*, **64**, 2332–2354.
- Bergman, J. W., H. H. Hendon, and K. M. Weickmann, 2001: Intraseasonal air-sea interactions at the onset of El Niño. *J. Climate*, **14**, 1702–1719.
- Bessafi, M., and M. Wheeler, 2006: Modulation of south Indian Ocean tropical cyclones by the Madden-Julian oscillation and convectively coupled equatorial waves. *Mon. Wea. Rev.*, **134**, 638–656.
- Bracco, A., F. Kucharski, F. Molteni, W. Hazleger, and C. Severijns, 2006: A recipe for simulating the interannual variability of the Asian summer monsoon and its relation with ENSO. *Climate Dyn.*, **28**, 441–460.
- Camargo, S., M. Wheeler, and A. Sobel, 2009: Diagnosis of the MJO modulation of tropical cyclogenesis using an empirical index. *J. Atmos. Sci.*, **66**, 3061–3074.
- Cassou, C., 2008: Intraseasonal interaction between the Madden-Julian oscillation and the North Atlantic Oscillation. *Nature*, **455**, 523–527.
- Chakraborty, A., and T. N. Krishnamurti, 2003: A coupled model study on ENSO, MJO and Indian summer monsoon rainfall relationships. *Meteor. Atmos. Phys.*, **84**, 243–254.
- Cherchi, A., S. Gualdi, S. Behera, J. J. Luo, S. Masson, T. Yamagata, and A. Navarra, 2007: The influence of tropical Indian Ocean SST on the Indian summer monsoon. *J. Climate*, **20**, 3083–3105.
- Danabasoglu, G., S. Bates, B. Briegleb, S. Jayne, M. Jochum, W. Large, S. Peacock, and S. Yeager, 2012: The CCSM4 ocean component. *J. Climate*, in press.

- Gent, P. R., and Coauthors, 2011: The Community Climate System Model version 4. *J. Climate*, **24**, 4973–4991.
- Goswami, B., and R. Mohan, 2001: Intraseasonal oscillations and interannual variability of the Indian summer monsoon. *J. Climate*, **14**, 1180–1198.
- , V. Krishnamurthy, and H. Annmalai, 1999: A broad-scale circulation index for the interannual variability of the Indian summer monsoon. *Quart. J. Roy. Meteor. Soc.*, **125**, 611–633.
- , R. Ajayamohan, P. Xavier, and D. Sengupta, 2003: Clustering of synoptic activity by Indian summer monsoon intraseasonal oscillations. *Geophys. Res. Lett.*, **30**, 1431, doi:10.1029/2002GL016734.
- Gregory, D., R. Kershaw, and P. M. Inness, 1997: Parametrization of momentum transport by convection. II: Tests in single-column and general circulation models. *Quart. J. Roy. Meteor. Soc.*, **123**, 1153–1183.
- Hendon, H. H., and M. Wheeler, 2008: Some space–time spectral analyses of tropical convection and planetary-scale waves. *J. Atmos. Sci.*, **65**, 2936–2948.
- , —, and C. Zhang, 2007: Seasonal dependence of the MJO–ENSO relationship. *J. Climate*, **20**, 531–543.
- Huffman, G. J., R. F. Adler, M. M. Morrissey, D. T. Bolvin, S. Curtis, R. Joyce, B. Mcgavock, and J. Susskind, 2001: Global precipitation at one-degree daily resolution from multisatellite observations. *J. Hydrometeorol.*, **2**, 36–50.
- Ihara, C., Y. Kushnir, M. A. Cane, and V. H. De La Peña, 2007: Indian summer monsoon rainfall and its link with ENSO and Indian Ocean climate indices. *Int. J. Climatol.*, **27**, 179–187.
- Inness, P. M., J. M. Slingo, E. Guilyardi, and J. Cole, 2003: Simulation of the Madden–Julian oscillation in a coupled general circulation model. Part II: The role of the basic state. *J. Climate*, **16**, 365–382.
- Jochum, M., 2009: Impact of latitudinal variations in vertical diffusivity on climate simulations. *J. Geophys. Res.*, **114**, C01010, doi:10.1029/2008JC005030.
- Ju, J., and J. Slingo, 1995: The Asian summer monsoon and ENSO. *Quart. J. Roy. Meteor. Soc.*, **121**, 1133–1168.
- Kalnay, E., and Coauthors, 1996: The NCEP/NCAR 40-Year Reanalysis Project. *Bull. Amer. Meteor. Soc.*, **77**, 437–471.
- Kessler, W., 2001: EOF representations of the Madden–Julian oscillation and its connection with ENSO. *J. Climate*, **14**, 3055–3061.
- , and R. Kleeman, 2000: Rectification of the Madden–Julian oscillation into the ENSO cycle. *J. Climate*, **13**, 3560–3575.
- Kiladis, G. N., M. C. Wheeler, P. T. Haertel, K. H. Straub, and P. E. Roundy, 2009: Convectively coupled equatorial waves. *Rev. Geophys.*, **47**, RG2003, doi:10.1029/2008RG000266.
- Kim, D., and Coauthors, 2009: Application of MJO simulation diagnostics to climate models. *J. Climate*, **22**, 6413–6436.
- Krishnamurthy, V., and B. Kirtman, 2003: Variability of the Indian Ocean: Relation to monsoon and ENSO. *Quart. J. Roy. Meteor. Soc.*, **129**, 1623–1646.
- Kug, J., K. Sooraj, F. Jin, and J. Luo, 2009: Impact of Indian Ocean dipole on high-frequency atmospheric variability over the Indian Ocean. *Atmos. Res.*, **94**, 134–139.
- Large, W. G., and S. Yeager, 2009: The global climatology of an interannually varying air-sea flux dataset. *Climate Dyn.*, **33**, 341–364.
- Lau, W. K. M., 2005: El Niño Southern Oscillation connection. *Intraseasonal Variability in the Atmosphere-Ocean Climate System*, W. K. M. Lau and D. Waliser, Eds., Praxis Publishing, 271–305.
- , and D. Waliser, Eds., 2005: *Intraseasonal Variability in the Atmosphere-Ocean Climate System*. Praxis Publishing, 436 pp.
- Liebmann, B., and C. Smith, 1996: Description of a complete (interpolated) outgoing longwave radiation dataset. *Bull. Amer. Meteor. Soc.*, **77**, 1275–1277.
- , H. Hendon, and J. Glick, 1994: The relationship between tropical cyclones of the western Pacific and Indian Oceans and the Madden–Julian oscillation. *J. Meteor. Soc. Japan*, **72**, 401–412.
- Lin, A., and T. Li, 2008: Energy spectrum characteristics of boreal summer intraseasonal oscillations: Climatology and variations during the ENSO developing and decaying phases. *J. Climate*, **21**, 6304–6320.
- Lin, J.-L., and Coauthors, 2006: Tropical intraseasonal variability in 14 IPCC AR4 climate models. Part I: Convective signals. *J. Climate*, **19**, 2665–2690.
- , M.-I. Lee, D. Kim, I.-S. Kang, and D. M. W. Frierson, 2008: The impacts of convective parameterization and moisture triggering on AGCM-simulated convectively coupled equatorial waves. *J. Climate*, **21**, 883–909.
- Lin, S., 2004: A “vertically Lagrangian” finite-volume dynamical core for global models. *Mon. Wea. Rev.*, **132**, 2293–2307.
- Madden, R., and P. Julian, 1971: Detection of a 40–50 day oscillation in the zonal wind in the tropical Pacific. *J. Atmos. Sci.*, **28**, 702–708.
- , and —, 1972: Description of global-scale circulation cells in the tropics with a 40–50 day period. *J. Atmos. Sci.*, **29**, 1109–1123.
- , and —, 1994: Observations of the 40–50-day tropical oscillation—A review. *Mon. Wea. Rev.*, **122**, 814–837.
- Maloney, E. D., and D. L. Hartmann, 2000a: Modulation of eastern North Pacific hurricanes by the Madden–Julian oscillation. *J. Climate*, **13**, 1451–1460.
- , and —, 2000b: Modulation of hurricane activity in the Gulf of Mexico by the Madden–Julian oscillation. *Science*, **287**, 2002–2004.
- Marshall, A. G., O. Alves, and H. H. Hendon, 2009: A coupled GCM analysis of MJO activity at the onset of El Niño. *J. Atmos. Sci.*, **66**, 966–983.
- Neale, R., J. Richter, and M. Jochum, 2008: The impact of convection on ENSO: From a delayed oscillator to a series of events. *J. Climate*, **21**, 5904–5924.
- Newman, M., P. Sardeshmukh, and C. Penland, 2009: How important is air-sea coupling in ENSO and MJO evolution? *J. Climate*, **22**, 2958–2977.
- Pai, D. S., J. Bhate, O. P. Sreejith, and H. R. Hatwar, 2011: Impact of MJO on the intraseasonal variation of summer monsoon rainfall over India. *Climate Dyn.*, **36**, 41–55.
- Pohl, B., N. Fauchereau, C. J. C. Reason, and M. Rouault, 2010: Relationships between the Antarctic Oscillation, the Madden–Julian oscillation, and ENSO, and consequences for rainfall analysis. *J. Climate*, **23**, 238–254.
- Rao, S., S. Masson, J. Luo, S. Behera, and T. Yamagata, 2007: Termination of Indian Ocean dipole events in a coupled general circulation model. *J. Climate*, **20**, 3018–3035.
- Raymond, D., and A. M. Blyth, 1986: A stochastic mixing model for nonprecipitating cumulus clouds. *J. Atmos. Sci.*, **43**, 2708–2718.
- , and —, 1992: Extension of the stochastic mixing model to cumulonimbus clouds. *J. Atmos. Sci.*, **49**, 1968–1983.
- Richter, J., and P. J. Rasch, 2008: Effects of convective momentum transport on the atmospheric circulation in the Community Atmosphere Model, version 3. *J. Climate*, **21**, 1487–1499.
- Roundy, P., 2008: Analysis of convectively coupled Kelvin waves in the Indian Ocean MJO. *J. Atmos. Sci.*, **65**, 1342–1359.

- , and J. R. Kravitz, 2009: The association of the evolution of intraseasonal oscillations to ENSO phase. *J. Climate*, **22**, 381–395.
- , C. J. Schreck III, and M. A. Janiga, 2009: Contributions of convectively coupled equatorial Rossby waves and Kelvin waves to the real-time multivariate MJO indices. *Mon. Wea. Rev.*, **137**, 469–478.
- Saji, N., B. Goswami, P. Vinayachandran, and T. Yamagata, 1999: A dipole mode in the tropical Indian Ocean. *Nature*, **401**, 360–363.
- Sardeshmukh, P., and P. Sura, 2007: Multiscale impacts of variable heating in climate. *J. Climate*, **20**, 5677–5695.
- Slingo, J., and H. Annamalai, 2000: 1997: The El Niño of the century and the response of the Indian summer monsoon. *Mon. Wea. Rev.*, **128**, 1778–1797.
- , and P. Inness, 2005: Modelling the MJO. *Intraseasonal Variability in the Atmosphere-Ocean Climate System*, D. Waliser and W. Lau, Eds., Praxis Publishing, 361–383.
- , and Coauthors, 1996: Intraseasonal oscillations in 15 atmospheric general circulation models: Results from an AMIP diagnostic subproject. *Climate Dyn.*, **12**, 325–358.
- Sperber, K., and H. Annamalai, 2008: Coupled model simulations of boreal summer intraseasonal (30–50 day) variability, part 1: Systematic errors and caution on use of metrics. *Climate Dyn.*, **31**, 345–372.
- Takayabu, Y., T. Iguchi, M. Kachi, A. Shibata, and H. Kanzawa, 1999: Abrupt termination of the 1997–98 El Niño in response to a Madden-Julian oscillation. *Nature*, **402**, 279–282.
- Tang, Y., and B. Yu, 2008: MJO and its relationship to ENSO. *J. Geophys. Res.*, **113**, D14106, doi:10.1029/2007JD009230.
- Waliser, D. E., 2006a: Intraseasonal variability. *The Asian Monsoon*, B. Wang, Ed., Springer Praxis, 203–257.
- , 2006b: Predictability of tropical intraseasonal variability. *Predictability of Weather and Climate*, T. Palmer and R. Hagedorn, Eds., Cambridge University Press, 275–305.
- , and Coauthors, 2003: AGCM simulations of intraseasonal variability associated with the Asian summer monsoon. *Climate Dyn.*, **21**, 423–446.
- , and Coauthors, 2009: MJO simulation diagnostics. *J. Climate*, **22**, 3006–3030.
- Walker, G. T., 1923: Correlation in seasonal variations of weather, VIII: A preliminary study of world-weather. *Mem. India Meteor. Dep.*, **24**, 75–131.
- , 1924: Correlation in seasonal variations of weather, IX: A further study of world weather. *Mem. India Meteor. Dep.*, **24**, 275–333.
- Webster, P., and S. Yang, 1992: Monsoon and ENSO: Selectively interactive systems. *Quart. J. Roy. Meteor. Soc.*, **118**, 877–926.
- , A. Moore, J. Loschnigg, and R. Leben, 1999: Coupled ocean-atmosphere dynamics in the Indian Ocean during 1997–98. *Nature*, **401**, 356–360.
- Wheeler, M. C., and H. H. Hendon, 2004: An all-season real-time multivariate MJO index: Development of an index for monitoring and prediction. *Mon. Wea. Rev.*, **132**, 1917–1932.
- , and J. L. McBride, 2005: Australian-Indonesian monsoon. *Intraseasonal Variability in the Atmosphere-Ocean Climate System*, W. K. M. Lau and D. E. Waliser Eds., Praxis Publishing, 125–173.
- Xie, P., and P. Arkin, 1997: Global precipitation: A 17-year monthly analysis based on gauge observations, satellite estimates, and numerical model outputs. *Bull. Amer. Meteor. Soc.*, **78**, 2539–2558.
- Yasunari, T., 1979: Cloudiness fluctuations associated with the Northern Hemisphere summer monsoon. *J. Meteor. Soc. Japan*, **57**, 227–242.
- Yuan, Y., H. Yang, W. Zhou, and C. Li, 2008: Influences of the Indian Ocean dipole on the Asian summer monsoon in the following year. *Int. J. Climatol.*, **28**, 1849–1859.
- Zavalá-Garay, J., C. Zhang, A. Moore, and R. Kleeman, 2005: The linear response of ENSO to the Madden-Julian oscillation. *J. Climate*, **18**, 2441–2459.
- Zhang, C., 2005: Madden-Julian oscillation. *Rev. Geophys.*, **43**, 1–36.
- , M. Dong, S. Gualdi, H. Hendon, and E. Maloney, 2006: Simulations of the Madden-Julian oscillation in four pairs of coupled and uncoupled global models. *Climate Dyn.*, **27**, 573–592.
- Zhang, G. J., 2003: Convective quasi-equilibrium in the tropical western Pacific: Comparison with midlatitude continental environment. *J. Geophys. Res.*, **108**, 4592, doi:10.1029/2003JD003520.
- , and N. A. McFarlane, 1995: Role of convective scale momentum transport in climate simulation. *J. Geophys. Res.*, **100**, 1417–1426.
- Zhou, L., R. Neale, M. Jochum, and R. Murtugudde, 2012: Improved Madden-Julian oscillations with improved physics: The impact of modified convection parameterizations. *J. Climate*, in press.